

# Higher-Order Spectra of Weak Lensing Convergence Maps in Parameterized Theories of Modified Gravity

D. Munshi, J. D. McEwen

*Mullard Space Science Laboratory, University College London, Holmbury St Mary, Dorking, Surrey RH5 6NT, UK*

14 March 2024

## ABSTRACT

We compute the low- $\ell$  limit of the family of higher-order spectra for projected (2D) weak lensing convergence maps. In this limit these spectra are computed to an arbitrary order using *tree-level* perturbative calculations. We use the flat-sky approximation and Eulerian perturbative results based on a generating function approach. We test these results for the lower-order members of this family, i.e. the skew- and kurt-spectra against state-of-the-art simulated all-sky weak lensing convergence maps and find our results to be in very good agreement. We also show how these spectra can be computed in the presence of a realistic sky-mask and Gaussian noise. We generalize these results to three-dimensions (3D) and compute the *equal-time* higher-order spectra. These results will be valuable in analyzing higher-order statistics from future all-sky weak lensing surveys such as the *Euclid* survey at low- $\ell$  modes. As illustrative examples, we compute these statistics in the context of the *Horndeski* and *Beyond Horndeski* theories of modified gravity. They will be especially useful in constraining theories such as the Gleyzes-Langlois-Piazza-Vernizzi (GLPV) theories and Degenerate Higher-Order Scalar-Tensor (DHOST) theories as well as the commonly used normal-branch of Dvali-Gabadadze-Porrati (nDGP) model, clustering quintessence models and scenarios with massive neutrinos.

**Key words:** : Cosmology– Weak Lensing– Methods: analytical, statistical, numerical

## 1 INTRODUCTION

We have a standard model of cosmology thanks to recently completed Cosmic Microwave Background Radiation (CMBR) experiments such as the *Planck* Surveyor<sup>1</sup> (Planck Collaboration 2013, 2016, 2018). However, many of the outstanding questions pertaining , e.g. to the nature of dark matter and dark energy or possible modification of General Relativity on cosmological scales remain unanswered (Joyce et al. 2015; Clifton et al. 2012). In addition they will also provide an estimate of the sum of the neutrino masses (Lesgourgues & Pastor 2006). Ongoing and planned future large scale structure (LSS) surveys may resolve or will provide clues for these questions using weak lensing analyses. Observational programs of many such surveys, including *Euclid*<sup>2</sup> (Laureijs et al. 2011), CFHTLS<sup>3</sup>, PAN-

<sup>1</sup> Planck

<sup>2</sup> <http://sci.esa.int/euclid/>

<sup>3</sup> <http://www.cfht.hawaii.edu/Sciences/CFHLS>

STARRS<sup>4</sup>, Dark Energy Surveys (DES)<sup>5</sup> (Abott et al. 2016), WiggleZ<sup>6</sup> (Jurek et al. 2010), LSST<sup>7</sup> (Tyson et al. 2003), BOSS<sup>8</sup> (Eisenstein et al. 2011), KiDS (Kuijken et al. 2015) and WFIRST (National Research Council 2010) lists weak lensing as their main science driver.

From the early days of detection the weak lensing (Munshi et al. 2008) studies have matured to a point where weak lensing results from *Euclid* are expected to constrain the cosmological parameters to sub-percent accuracy. However, weak lensing at smaller angular scales probes the nonlinear regime of gravitational clustering, and is thus key to understanding the non-Gaussianity induced by the nonlinearity and fully exploiting in the weak lensing maps. The higher-order statistics are also useful for the breaking of parameter degeneracies in studies involving the power spectrum analysis alone and they are also important in understanding the variance or error of estimation of lower-order statistics. These higher-order statistics including the cumulants (Bernardeau 1994) and their correlators (Bernardeau 1996; Munshi et al. 2012; Riquelme & Spergel 2012; Calabrese et al. 2010) are among the best-known diagnostics of the deviation from Gaussianity that characterizes the non-linear regime (Bartolo et al. 2004), with a long history analytical modeling (Bernardeau et al. 2002). Most of these studies use extensions of perturbative results in the quasilinear regime valid at large smoothing angular scales or variants of halo models (Cooray & Sheth 2002). Early studies concentrated on measurements of higher-order correlation hierarchy in the angular space due to small survey size (Bernardeau et al. 2002; Bernardeau, Waerbeke, Mellier 2003). However, the near all-sky coverage of future surveys such as *Euclid* will let us estimate higher-order statistics in the harmonic domain with unprecedented accuracy (Amendola et al. 2013). While measurements of real space correlations are much simpler in the presence of complicated survey design the measurements for different angular scales can be highly correlated (Munshi & Jain 2000; Munshi 2000). In comparison measurements in the harmonic domain are less correlated and each mode contains (nearly) independent information in the limit of all-sky coverage. The primary motivation of this study is to develop analytical predictions for one such statistic called the skew-spectrum, and test them against numerical simulations. We will borrow the concepts developed for constructing skew-spectra for the study of non-Gaussianity in the context of CMBR observations (Planck Collaboration 2016). However, we also include gravity-induced secondary non-Gaussianity. The skew-spectrum is the lowest-order member in the family of higher-order spectra (Munshi et al. 2011a,b). In a series of papers the one-point statistics such as the skewness and kurtosis were generalized to two-point cumulant correlator, e.g. the two-to-one correlator and its higher-order generalizations. These can be represented in the harmonic domain by their associated spectra such as the skew-spectrum (Munshi & Heavens 2010) and its higher-order generalizations (Munshi et al. 2011a,b). These spectra have already been used to analyze WMAP<sup>9</sup> (Smidt et al. 2012) as well as *Planck* data (Planck Collaboration 2016). They are useful tools to separate individual contributions and estimate systematics. In this paper we will concentrate on the projected skew-spectrum and kurt-spectrum in the context of weak lensing surveys (Munshi et al. 2011).

Other similar estimators also exist, including the morphological estimators (Munshi et al. 2012), e.g. position-dependent power spectra (Munshi 2017), phase correlations (Matsubara 2007), line-correlations (Eggemeier & Smith 2012), peak-statistics (Peel et al. 2012), peak-correlations (Heavens & Gupta 2012) and extreme value statistics (Harrison & Coles 2012).

Many modified gravity theories are now severely constrained with the first detection of GW170817 (Abott et al. 2017) and its electromagnetic counterpart GRB 170817A (Goldstein et al. 2017) implying Gravity Waves travel at the speed of light with deviation smaller than  $\text{few} \times 10^{-15}$  - see e.g. Baker et al. (2017); Sakstein & Jain (2017); Lombriser & Lima (2017); Creminelli & Vernizzi (2017). However, some of the models we consider here are designed to evade this constraint. It is expected that the constraints on these models will be further tightened by the observations of large scale structure by *Euclid* and LSST. The higher-order statistics we develop here can be very effectively used to test these models independently or jointly with power spectrum estimates. As a concrete example of the higher-order spectra we take the modified gravity theories also known as the Horndeski's theory of gravity. These are the most general theory of gravity that has second-order equation of motion. It was proposed first in 1974 (Barthelemy 2019) and since then, it was realised that Horndeski theory contains many other theories of gravity as a special cases. These include General relativity, Jordon-Brans-Dicke theories of gravity, Dilaton and Chameleon theories of gravity, theories involving as co-variant Galileons as well as models of Quintessence. All of these models of gravity have found use in construction of cosmological models of inflation as well as dark energy (see e.g. Deffayet et al (2011); Barthelemy (2019); Gleyzes et al. (2015a,b); Langois & Noui (2016a,b) for an incomplete list of recent references). We use a recent parametrization of the gravity induced bispectrum in this model as well as models that are known as the beyond Horndeski theories to compute the skew-spectrum in the low- $\ell$  limit.

<sup>4</sup> <http://pan-starrs.ifa.hawaii.edu/>

<sup>5</sup> <https://www.darkenergysurvey.org/>

<sup>6</sup> <http://wigglez.swin.edu.au/>

<sup>7</sup> [http://www.lsst.org/llst\\_home.shtml](http://www.lsst.org/llst_home.shtml)

<sup>8</sup> <http://www.sdss3.org/surveys/boss.php>

<sup>9</sup> <https://map.gsfc.nasa.gov/>

This paper is organized as follows. In §2 we review results regarding the convergence bispectrum in the context of tree-level Standard Perturbation Theory (SPT). In §3 we introduce the skew-spectrum and relate it to the bispectrum. The corresponding results for trispectrum and kurt-spectra are derived in §4. Theoretical predictions in the context of generating functions are derived in §5. The generalization of higher-order spectra is presented in §6. The higher-order spectra can be derived in the presence of a mask. The corresponding results are presented in §7. The simulations are discussed in §8, the numerical results are presented in §9. We present the results for various modified gravity and other beyond- $\Lambda$ CDM scenarios in §10. Finally, the conclusions are drawn in §11.

## 2 MODELLING OF HIGHER-ORDER WEAK LENSING SPECTRA

In this section we will review the aspects of standard tree-level perturbative which we use to compute the bispectrum as well trispectrum as and eventually the skew-spectrum and kurt-spectrum.

### 2.1 Tree-level Perturbative Calculations

In the quasilinear regime ( $\delta \leq 1$ ), the evolution of density contrast  $\delta$  can be described using SPT (Munshi et al. 2008). However, the treatment based on perturbation theory breaks down when density contrast at a given length scale becomes nonlinear ( $\delta \geq 1$ ) which significantly increases the growth of clustering. We will denote the Fourier transform of the density contrast  $\delta(\mathbf{r})$  by  $\delta(\mathbf{k})$ , where  $\mathbf{r}$  is the comoving co-ordinate, and  $\mathbf{k}$  denotes the comoving wavenumber. Expanding the  $\delta(\mathbf{k})$ , in a perturbative series, and assuming the density contrast is less than unity, for the perturbative series to be convergent, we get:

$$\delta(\mathbf{k}) = \delta^{(1)}(\mathbf{k}) + \delta^{(2)}(\mathbf{k}) + \delta^{(3)}(\mathbf{k}) + \dots, \quad (1a)$$

The  $n$ -th order perturbative term denoted as  $\delta^{(n)}$  is  $\propto [\delta^{(1)}]^n$  where  $\delta^{(1)}$  is the linear density contrast. The term  $\delta^{(n)}$  is expressed using a kernel  $F_n$  using the following convolution:

$$\delta^{(n)}(\mathbf{k}) = \int d\mathbf{k}_1 \dots \int d\mathbf{k}_n \delta_{3D}(\mathbf{k}_1 + \dots + \mathbf{k}_n - \mathbf{k}) F_n(\mathbf{k}_1, \dots, \mathbf{k}_n) \delta^{(1)}(\mathbf{k}_1) \dots \delta^{(1)}(\mathbf{k}_n); \quad d\mathbf{k} = \frac{d^3\mathbf{k}}{(2\pi)^{3/2}}. \quad (1b)$$

The Dirac delta function in 3D is denoted by  $\delta_{3D}$  and  $\mathbf{k}_1, \mathbf{k}_2, \dots, \mathbf{k}_n$  denotes different wavenumbers. The second-order kernel  $F_2$  has the following expression. For the higher-order kernels see (Munshi et al. 2008):

$$F_2(\mathbf{k}_1, \mathbf{k}_2) = \frac{5}{7} + \frac{1}{2} \left( \frac{k_1}{k_2} + \frac{k_2}{k_1} \right) \left( \frac{\mathbf{k}_1 \cdot \mathbf{k}_2}{k_1 k_2} \right) + \frac{2}{7} \left( \frac{\mathbf{k}_1 \cdot \mathbf{k}_2}{k_1 k_2} \right)^2, \quad k_i = |\mathbf{k}_i|. \quad (1c)$$

Throughout we will use the following convention for the three-dimensional (3D) Fourier Transform (FT) and its inverse:

$$\delta(\mathbf{k}) = \int d\mathbf{r} \exp(-i\mathbf{k} \cdot \mathbf{r}) \delta(\mathbf{r}); \quad \delta(\mathbf{r}) = \int d\mathbf{k} \exp(i\mathbf{k} \cdot \mathbf{r}) \delta(\mathbf{k}); \quad d\mathbf{r} = \frac{d^3\mathbf{r}}{(2\pi)^{3/2}}. \quad (2)$$

We have suppressed the temporal dependence in Eq.(1a)-Eq.(1b) which will be introduced later in this section. The power spectrum  $P_\delta$  and the bispectrum  $B_\delta$  of  $\delta$  are defined respectively as the two and three point correlation of the variable  $\delta(\mathbf{k})$ . The  $P_{\text{lin}}(k)$  denotes the linear power spectrum, i.e.  $\delta_{\text{lin}}(\mathbf{k}) = \delta^{(1)}(\mathbf{k})$  and  $\langle \delta_{\text{lin}}(\mathbf{k}_1) \delta_{\text{lin}}(\mathbf{k}_2) \rangle_c = (2\pi)^3 \delta_{3D}(\mathbf{k}_1 + \mathbf{k}_2) P_{\text{lin}}(k_1)$ . Throughout angular brackets represent ensemble averaging. The subscript  $\text{lin}$  stands for linear-order contributions.

The linearized solution for the density field is  $\delta^{(1)}(\mathbf{k})$ ; higher-order terms yield corrections to this linear solution. Using an *ideal* fluid approach known to be valid at large scales (and before shell crossing) one can write the second order correction to the linearized density field using the kernel  $F_2(\mathbf{k}_1, \mathbf{k}_2)$ . The cosmological structure formation is described by a set of equation which describes the Newtonian gravity coupled to the Euler and continuity equation (Munshi et al. 2008). This system of non-linear, coupled integro-differential equations are used to compute the kernels  $F_2(\mathbf{k}_1, \mathbf{k}_2)$ ,  $F_3(\mathbf{k}_1, \mathbf{k}_2, \mathbf{k}_3)$  and their high-order counterparts. This is typically done perturbatively in an order-by-order manner.

## 2.2 Weak Lensing Statistics in Projection (2D)

We will now specialize our discussion to weak lensing surveys. The weak lensing convergence  $\kappa$  is a line of sight projection of the 3D density contrast  $\delta(\mathbf{r})$ :

$$\kappa(\hat{\Omega}; r_s) = \int_0^{r_s} dr w(r, r_s) \delta(r, \hat{\Omega}); \quad w(r, r_s) = \frac{3\Omega_M}{2} \frac{H_0^2}{ac^2} \frac{d_A(r)d_A(r_s - r)}{d_A(r_s)}. \quad (3)$$

Where  $r$  is the comoving distance,  $\hat{\Omega} = (\theta, \phi)$  is a unit vector that defines the position of the ppxel on the surface of the sky, with  $\theta$  and  $\phi$  respectively representing the azimuthal and polar co-ordinates  $d\hat{\Omega} = \sin\theta d\theta d\phi$  is the measure of integration,  $r_s$  is the radial comoving distance to the source plane,  $c$  is the speed of light,  $a$  represents the scale factor,  $H_0$  the Hubble parameter,  $d_A(r)$  is the comoving angular diameter distance and the three-dimensional (3D) density contrast  $\delta$  and  $\Omega_M$  is the cosmological density parameter. We will ignore the source distribution and assume them to be localized on a single source plane, we will also ignore photometric redshift errors. However, such complications are essential to link predictions to observational data and can readily be included in our analysis. To avoid cluttering, we will suppress the  $r_s$  dependence of  $\kappa(\hat{\Omega}, r_s)$  and  $w(r, r_s)$  defined in Eq.(1a) in the following. The corresponding 3D power spectrum  $P_\delta$ , bispectrum  $B_\delta$  and trispectrum  $T_\delta$  for  $\delta$  are:

$$\langle \delta(\mathbf{k}_1) \delta(\mathbf{k}_2) \rangle_c = (2\pi)^3 \delta_{3D}(\mathbf{k}_1 + \mathbf{k}_2) P_\delta(k_1); \quad k = |\mathbf{k}|; \quad (4a)$$

$$\langle \delta(\mathbf{k}_1) \delta(\mathbf{k}_2) \delta(\mathbf{k}_3) \rangle_c = (2\pi)^3 \delta_{3D}(\mathbf{k}_1 + \mathbf{k}_2 + \mathbf{k}_3) B_\delta(\mathbf{k}_1, \mathbf{k}_2, \mathbf{k}_3); \quad (4b)$$

$$\langle \delta(\mathbf{k}_1) \cdots \delta(\mathbf{k}_4) \rangle_c = (2\pi)^3 \delta_{3D}(\mathbf{k}_1 + \cdots + \mathbf{k}_4) T_\delta(\mathbf{k}_1, \cdots, \mathbf{k}_3). \quad (4c)$$

The subscript  $c$  denotes the fact that only connected diagrams are included in computing these statistics. The flat-sky power spectrum  $P^\kappa$  and bispectrum  $B^\kappa$  are similarly defined through (Munshi et al. 2008):

$$\langle \kappa(\mathbf{l}_1) \kappa(\mathbf{l}_2) \rangle_c = (2\pi)^2 \delta_{2D}(\mathbf{l}_1 + \mathbf{l}_2) P^\kappa(l_1); \quad (5a)$$

$$\langle \kappa(\mathbf{l}_1) \kappa(\mathbf{l}_2) \kappa(\mathbf{l}_3) \rangle_c = (2\pi)^2 \delta_{2D}(\mathbf{l}_1 + \mathbf{l}_2 + \mathbf{l}_3) B^\kappa(\mathbf{l}_1, \mathbf{l}_2, \mathbf{l}_3); \quad (5b)$$

$$\langle \kappa(\mathbf{l}_1) \cdots \kappa(\mathbf{l}_4) \rangle_c = (2\pi)^2 \delta_{2D}(\mathbf{l}_1 + \cdots + \mathbf{l}_3) T^\kappa(\mathbf{l}_1, \mathbf{l}_2, \mathbf{l}_3, \mathbf{l}_4). \quad (5c)$$

The wavenumbers  $\mathbf{l}, \mathbf{l}_1, \cdots, \mathbf{l}_4$  are wavenumbers defined on the flat-patch of the sky. For a given radial distance  $r$  they are related to the projected 3D wave number by the relation  $\mathbf{l} = \mathbf{k}_\perp / d_A(r)$ ; where  $d_A(r)$  being the co-moving angular diameter distance defined before and  $l = |\mathbf{l}|$ . Using the *flat-sky* approximation as well as *Limber* and *prefactor unity* approximation the projected power spectrum  $P^\kappa(l)$  and bispectrum  $B^\kappa(\mathbf{k}_1, \mathbf{k}_2, \mathbf{k}_3)$  can be expressed respectively in terms of the 3D  $\delta$  power spectrum  $P_\delta(k)$  and bispectrum  $B_\delta(\mathbf{k}_1, \mathbf{k}_2, \mathbf{k}_3)$  (Munshi et al. 2008):

$$P^\kappa(l) = \int_0^{r_s} dr \frac{\omega^2(r)}{d_A^2(r)} P_\delta\left(\frac{l}{d_A(r)}; r\right); \quad (6a)$$

$$B^\kappa(\mathbf{l}_1, \mathbf{l}_2, \mathbf{l}_3) = \int_0^{r_s} dr \frac{\omega^3(r)}{d_A^4(r)} B_\delta\left(\frac{\mathbf{l}_1}{d_A(r)}, \frac{\mathbf{l}_2}{d_A(r)}, \frac{\mathbf{l}_3}{d_A(r)}; r\right); \quad (6b)$$

$$T^\kappa(\mathbf{l}_1, \mathbf{l}_2, \mathbf{l}_3, \mathbf{l}_4) = \int_0^{r_s} dr \frac{\omega^4(r)}{d_A^6(r)} T_\delta\left(\frac{\mathbf{l}_1}{d_A(r)}, \frac{\mathbf{l}_2}{d_A(r)}, \frac{\mathbf{l}_3}{d_A(r)}, \frac{\mathbf{l}_4}{d_A(r)}; r\right). \quad (6c)$$

The superscript  $\kappa$  correspond to the convergence field which these statistics correspond to. The function  $\omega$  is defined in Eq.(3). We will use different approximations introduced in §2 in Eq.(6a)-Eq.(6b) to compute the convergence or  $\kappa$  bispectrum.

## 3 BISPECTRUM AND SKEW-SPECTRUM

The spherical harmonic transform of a convergence map  $\kappa(\hat{\Omega})$ , denoted as  $\kappa_{\ell m}$ , defined over the surface of the sky using spherical harmonics  $Y_{\ell m}(\hat{\Omega})$  can be used to define the multipoles  $\kappa_{\ell m}$ :

$$\kappa_{\ell m} = \int d\hat{\Omega} Y_{\ell m}(\hat{\Omega}) \kappa(\hat{\Omega}); \quad \hat{\Omega} = (\theta, \varphi). \quad (7)$$

A Gaussian field is completely characterized by its power spectrum  $C_\ell^\kappa$  which is defined as  $C_\ell^\kappa = \langle \kappa_{\ell m} \kappa_{\ell m}^* \rangle$ . Here  $\kappa_{\ell m}^*$  represents the complex conjugate of  $\kappa_{\ell m}$ . The flat sky power spectrum  $P^\kappa(l)$  is identical to  $C_\ell^\kappa$  at high  $\ell$  with the identification  $l = \ell$ . Bispectrum is the

lowest order statistics that characterizes departure from Gaussianity that is defined as the three-point coupling of harmonic coefficients. Assuming isotropy and homogeneity the all-sky bispectrum  $B_{\ell_1 \ell_2 \ell_3}^\kappa$  is defined as (Bartolo et al. 2004):

$$\langle \kappa_{\ell_1 m_1} \kappa_{\ell_2 m_2} \kappa_{\ell_3 m_3} \rangle_c \equiv B_{\ell_1 \ell_2 \ell_3}^\kappa \begin{pmatrix} \ell_1 & \ell_2 & \ell_3 \\ m_1 & m_2 & m_3 \end{pmatrix}. \quad (8)$$

The quantity in parentheses is the well-known Wigner-3j symbol which enforces rotational invariance. It is only non-zero for the triplets  $(\ell_1, \ell_2, \ell_3)$  that satisfy the triangular condition and  $\ell_1 + \ell_2 + \ell_3$  is even. The reduced bispectrum  $b_{\ell_1 \ell_2 \ell_3}^\kappa$  for convergence  $\kappa$  is defined through the following expression (Bartolo et al. 2004):

$$B_{\ell_1 \ell_2 \ell_3}^\kappa = \sqrt{\frac{(2\ell_1 + 1)(2\ell_2 + 1)(2\ell_3 + 1)}{4\pi}} \begin{pmatrix} \ell_1 & \ell_2 & \ell_3 \\ 0 & 0 & 0 \end{pmatrix} b_{\ell_1 \ell_2 \ell_3}^\kappa. \quad (9)$$

The skew-spectrum is defined as the cross power spectrum formed by cross-correlating the squared  $\kappa^2$  maps against the original map  $\kappa$  (Munshi & Heavens 2010):

$$S_\ell^{(21)} = \frac{1}{2\ell + 1} \sum_m \text{Real}\{[\kappa^2]_{\ell m} [\kappa]_{\ell m}^*\} = \sum_{\ell_1 \ell_2} B_{\ell_1 \ell_2 \ell}^\kappa J_{\ell_1 \ell_2 \ell}; \quad (10a)$$

$$J_{\ell_1 \ell_2 \ell} = \sqrt{\frac{(2\ell_1 + 1)(2\ell_2 + 1)}{(2\ell + 1)}} \begin{pmatrix} \ell_1 & \ell_2 & \ell \\ 0 & 0 & 0 \end{pmatrix}. \quad (10b)$$

To avoid cluttering we will not explicitly display smoothing windows in our equations. The beam-smoothed versions of the expressions can be recovered by using the smoothed harmonics i.e. replacing  $\kappa_{\ell m}$  with  $\kappa_{\ell m} b_\ell$  where  $b_\ell$  is the smoothing beam in the harmonic domain which can be tophat or Gaussian. In case of Gaussian smoothing the expressions are derived in an order-by-order manner (Bernardeau 1994, 1996) For a tophat smoothing these expressions are derived using a generating function to an arbitrary order (Matsubara 2012). The normalized one-point skewness parameter (Bernardeau et al. 2002)  $S_3 = \langle \kappa^3 \rangle_c / \langle \kappa^2 \rangle_c^2$  can be recovered from the skew-spectrum by constructing the beam-smoothed third-order moment  $\langle \kappa^3 \rangle_c$  (Munshi & Heavens 2010)

$$\mu_3 = \langle \kappa^3 \rangle_c = \sum_\ell (2\ell + 1) S_\ell^{(21)} = \sum_{\ell_1 \ell_2 \ell} J_{\ell_1 \ell_2 \ell} B_{\ell_1 \ell_2 \ell}^\kappa. \quad (11)$$

The normalized skewness parameter  $S_3$  is defined as  $S_3 = \mu_3 / \mu_2^2$  with  $\mu_N = \langle \kappa^N \rangle_c$  and  $S_N = \mu_N / \mu_2^{N-1}$

The real space two-to-one correlation function can be defined in terms of the skew-spectrum as (Munshi & Heavens 2010):

$$\xi^{(21)}(\theta_{12}) = \langle \kappa^2(\hat{\Omega}_1) \kappa(\hat{\Omega}_2) \rangle_c = \frac{1}{4\pi} \sum_\ell (2\ell + 1) S_\ell^{(21)} P_\ell(\cos \theta_{12}). \quad (12)$$

Where  $P_\ell$  represents the Legendre Polynomial, and the angular positions  $\hat{\Omega}_1$  and  $\hat{\Omega}_2$  are separated by an angle  $\theta_{12}$ . Suitably normalized two-to-one correlator is the lowest order of a family of statistics also known as cumulant correlator (Bernardeau 1996; Munshi et al. 2012; Riquelme & Spergel 2012; Calabrese et al. 2010), which has also been used in the context of weak-lensing surveys (Munshi et al. 2012; Munshi 2000).

In our notation  $\delta_{2D}$  is the 2D Dirac delta function. The flat-sky bispectrum  $B^\kappa(\mathbf{l}_1, \mathbf{l}_2, \mathbf{l}_3)$  is identical to the reduced bispectrum  $b_{\ell_1 \ell_2 \ell_3}^\kappa$  for high multipole (Bartolo et al. 2004). This can be shown by noting the following asymptotic relationship.

$$\begin{aligned} \mathcal{G}_{\ell_1 m_1, \ell_2 m_2, \ell_3 m_3} &\equiv \int d\hat{\Omega} Y_{\ell_1 m_1}(\hat{\Omega}) Y_{\ell_2 m_2}(\hat{\Omega}) Y_{\ell_3 m_3}(\hat{\Omega}); \\ &= \sqrt{\frac{(2\ell_1 + 1)(2\ell_2 + 1)(2\ell_3 + 1)}{4\pi}} \begin{pmatrix} \ell_1 & \ell_2 & \ell_3 \\ 0 & 0 & 0 \end{pmatrix} \begin{pmatrix} \ell_1 & \ell_2 & \ell_3 \\ m_1 & m_2 & m_3 \end{pmatrix} \approx (2\pi)^2 \delta_{2D}(\mathbf{l}_1 + \mathbf{l}_2 + \mathbf{l}_3). \end{aligned} \quad (13)$$

A few comments about the skew-spectrum are in order. One-point statistics such as the skewness parameter have the advantage of having high signal-to-noise. However, they lack distinguishing power as all the available information in the bispectrum is compressed into a single number. In contrast, the skew-spectrum, encodes some information on the shape of the spectrum, and in principle can allow us to separate the contribution from gravity-induced non-Gaussianity or possible source of contamination from systematics. Though primordial non-Gaussianity is highly constrained in the light of *Planck* data, such contributions can also be tested using the skew-spectrum.

In this paper we consider a direct estimator for the skew-spectrum as opposed to the optimal estimator developed in (Munshi &

Heavens 2010) where optimality was achieved by using suitable weights to the harmonics that incorporates a match filtering as well as saturates the Cramer-Rao limit in the limit of weakly non-Gaussian limit. Indeed, a simple Fisher matrix based analysis, however, will non-longer be adequate for moderately non-Gaussian weak lensing maps. However, optimality is not of crucial importance of analysis for weak lensing maps as the secondary non-Gaussianity is expected to be detected with much higher signal-to-noise. A simpler direct estimator will thus be useful for studying non-Gaussianity in weak-lensing maps.

#### 4 TRISPECTRUM AND KURT-SPECTRA

The near all-sky weak lensing maps from surveys such as Euclid will also allow determination of non-Gaussianity statistics beyond the lowest-order, e.g. the fourth-order correlator or the trispectrum. Trispectrum can be useful not only to construct the covariance of the power spectrum estimator but also as a consistency check for the lower order estimators. In this section we will extend the estimator present above for the bispectrum to the case of trispectrum.

The trispectrum  $T_{\ell_3 \ell_4}^{\ell_1 \ell_2}(L)$  can be defined by the following expressions from the four-point correlation function of the spherical harmonics  $\kappa_{\ell m}$  for the convergence field  $\kappa$  (Munshi et al. 2011a):

$$\langle \kappa_{\ell_1 m_1} \kappa_{\ell_2 m_2} \kappa_{\ell_3 m_3} \kappa_{\ell_4 m_4} \rangle_c = \sum_{LM} (-1)^M T_{\ell_3 \ell_4}^{\ell_1 \ell_2}(L) \begin{pmatrix} \ell_1 & \ell_2 & L \\ m_1 & m_2 & M \end{pmatrix} \begin{pmatrix} \ell_3 & \ell_4 & L \\ m_3 & m_4 & -M \end{pmatrix}; \quad (14a)$$

$$T_{\ell_3 \ell_4}^{\ell_1 \ell_2}(L) = (2L+1) \sum_M \sum_{m_i} \begin{pmatrix} \ell_1 & \ell_2 & L \\ m_1 & m_2 & M \end{pmatrix} \begin{pmatrix} \ell_3 & \ell_4 & L \\ m_3 & m_4 & -M \end{pmatrix} \langle \kappa_{\ell_1 m_1} \kappa_{\ell_2 m_2} \kappa_{\ell_3 m_3} \kappa_{\ell_4 m_4} \rangle_c. \quad (14b)$$

Here,  $M$  is the magnetic quantum number associated with the azimuthal quantum number  $L$ . The Wigner 3j-symbols above ensure that the triangle inequalities imposed by statistical isotropy and homogeneity of the trispectrum in the harmonic space is represented by a quadrilateral. The harmonics  $\ell_1, \ell_2, \ell_3$  and  $\ell_4$  represent the sides of the quadrilateral and the harmonics  $L$  represents one of the diagonal of the quadrilateral. The two kurt-spectra  $\mathcal{K}_\ell^{(31)}$  and  $\mathcal{K}_\ell^{(31)}$  are defined as (Munshi et al. 2011a,b):

$$\mathcal{K}_\ell^{(31)} = \frac{1}{2\ell+1} \sum_m \text{Real}\{[\kappa^3]_{\ell m} [\kappa]_{\ell m}^*\} = \sum_{\ell_1 \ell_2 \ell_3 L} T_{\ell_1 \ell_2}^{\ell_3 \ell}(L) J_{\ell_1 \ell_2 L} J_{L \ell_3 \ell}; \quad (15a)$$

$$\mathcal{K}_\ell^{(22)} = \frac{1}{2\ell+1} \sum_m \{[\kappa^2]_{\ell m} [\kappa^2]_{\ell m}^*\} = \sum_{\ell_1 \ell_2 \ell_3 \ell_4} T_{\ell_1 \ell_2}^{\ell_3 \ell_4}(\ell) J_{\ell_1 \ell_2 \ell} J_{\ell_3 \ell_4 \ell}. \quad (15b)$$

Thus the kurt-spectra described above are computed using either by keeping the diagonal fixed and summing over all possible configurations (the two-to-two kurt-spectra  $\mathcal{K}_\ell^{(2,2)}$  defined in Eq.(15a)) or by keeping one of the side fixed and summing over all possible configurations (introduced above as three-to-one kurt-spectra  $\mathcal{K}_\ell^{(31)}$  defined in Eq.(15b)). These *states* are linked to the collapsed and squeezed configurations. At higher-order the polyspectra are characterized by a polygon. The number of polyspectra at a given order can be high since the number of diagonals and sides of such polygons can be quite high.

Another related point is that disconnected contributions will exist even in the absence of noise. These contributions need to be subtracted out when estimating from the data (Hu 2001; Okamoto & Hu 2002). The trispectrum in this case is given in Eq.(17) and is specified completely by the power spectrum  $\mathcal{C}_\ell$ . The corresponding spectra are given in terms of the Gaussian Trispectrum  $G_{\ell_3 \ell_4}^{\ell_1 \ell_2}(L)$  (Munshi et al. 2011a):

$$\mathcal{G}_\ell^{(31)} = \sum_{\ell_1 \ell_2 \ell_3 L} G_{\ell_1 \ell_2}^{\ell_3 \ell}(L) J_{\ell_1 \ell_2 L} J_{L \ell_3 \ell}; \quad \mathcal{G}_\ell^{(22)} = \sum_{\ell_1 \ell_2 \ell_3 \ell_4} G_{\ell_1 \ell_2}^{\ell_3 \ell_4}(\ell) J_{\ell_1 \ell_2 \ell} J_{\ell_3 \ell_4 \ell}. \quad (16)$$

where the Gaussian trispectrum  $G_{\ell_3 \ell_4}^{\ell_1 \ell_2}(L)$  is given by (Hu 2001; Okamoto & Hu 2002):

$$G_{\ell_3 \ell_4}^{\ell_1 \ell_2}(L) = (-1)^{\ell_1 + \ell_3} \sqrt{(2\ell_1 + 1)(2\ell_3 + 1)} \mathcal{C}_{\ell_1} \mathcal{C}_{\ell_3} \delta_{L0} \delta_{\ell_1 \ell_2} \delta_{\ell_2 \ell_3} \\ + (2L+1) \mathcal{C}_{\ell_1} \mathcal{C}_{\ell_2} [(-1)^{\ell_2 + \ell_3 + L} \delta_{\ell_1 \ell_3} \delta_{\ell_2 \ell_4} + \delta_{\ell_1 \ell_4} \delta_{\ell_2 \ell_3}]. \quad (17)$$

In (Munshi & Heavens 2010; Munshi et al. 2011a,b) optimal versions of skew- and kurt-spectra estimators were developed which requires weights based on target spectra. This method was used in investigating primordial spectra as the signal-to-noise is rather low.

However, for investigating the gravity induced secondary non-Gaussianity with surveys that have as high expected signal-to-noise as Euclid optimization is not mandatory.

The commonly used kurtosis parameter  $S_4$  (to be defined below) can be reconstructed from the kurt-spectra as follows (Munshi et al. 2011a):

$$\mu_4 = \langle \kappa^4(\hat{\Omega}) \rangle_c = \frac{1}{4\pi} \int \kappa^4(\hat{\Omega}) d\hat{\Omega} = \frac{1}{4\pi} \sum_L \sum_{\ell_1 \ell_2 \ell_3 \ell_4} h_{\ell_1 \ell_2 L} h_{\ell_3 \ell_4 L} T_{\ell_3 \ell_4}^{\ell_1 \ell_2}(L); \quad (18a)$$

$$= \sum_{\ell} (2\ell + 1) \mathcal{K}_{\ell}^{(31)} = \sum_{\ell} (2\ell + 1) \mathcal{K}_{\ell}^{(2,2)}. \quad (18b)$$

We will use noise free simulations but in case of analyzing noisy maps the  $\mathcal{C}_{\ell}$ s will also include the noise contribution. The commonly used kurtosis are normalized one-point estimators as (Bernardeau et al. 2002)  $S_4 = \left[ \frac{\mu_4 - 3\mu_2^2}{\mu_2^3} \right]$ . Here,  $\mu_2 = 1/4\pi \sum_{\ell} (2\ell + 1) \mathcal{C}_{\ell}$ . The corresponding cumulant correlators for these spectra are defined in a manner similar to Eq.(12) Munshi et al. (2011b):

$$\xi^{31}(\theta_{12}) = \langle \kappa^3(\hat{\Omega}_1) \kappa(\hat{\Omega}_2) \rangle_c = \frac{1}{4\pi} \sum_{\ell} (2\ell + 1) \mathcal{K}_{\ell}^{(31)} P_{\ell}(\cos \theta_{12}); \quad (19a)$$

$$\xi^{22}(\theta_{12}) = \langle \kappa^2(\hat{\Omega}_1) \kappa^2(\hat{\Omega}_2) \rangle_c = \frac{1}{4\pi} \sum_{\ell} (2\ell + 1) \mathcal{K}_{\ell}^{(22)} P_{\ell}(\cos \theta_{12}). \quad (19b)$$

Next we will employ tree-level perturbative calculations.

## 5 TREE-LEVEL PERTURBATIVE RESULTS

The unsmoothed normalized higher-order cumulants or  $S_N = \langle \delta^N \rangle_c / \langle \delta^2 \rangle_c^{N-1}$  can be expressed in terms of the tree-level vertices denoted as  $\nu_N$  using the following expressions (Bernardeau et al. 2002):

$$S_3 = 3\nu_2; \quad S_4 = 4\nu_3 + 12\nu_2^2; \quad S_5 = 5\nu_4 + 60\nu_3\nu_2 + 60\nu_2^3. \quad (20)$$

The vertices  $\nu_N$  are the angular averages of the mode-coupling kernels  $F_N$  defined in Eq.(1c) i.e.  $\nu_N = N! \langle F_N \rangle$  introduced in §2.2 in the Fourier domain.

$$\nu_N = N! \langle F_N \rangle = N! \int \frac{d\hat{\Omega}_{k_1}}{4\pi} \dots \int \frac{d\hat{\Omega}_{k_N}}{4\pi} F_N(\mathbf{k}_1, \dots, \mathbf{k}_N); \quad d\hat{\Omega}_k = \sin \theta_k d\theta_k d\varphi_k. \quad (21)$$

The following generating function approach was introduced in (Bernardeau 1992, 1994). The generating functions  $\mathcal{G}_{\delta}(\tau)$  are solved using the equations of gravitational dynamics encapsulated in Euler-Continuity-Poisson equations. Here  $\tau$  plays the role of a dummy variable. In the perturbative regime the  $\nu_N$  parameter can be computed for an arbitrary  $N$ .

$$\mathcal{G}_{\delta}(\tau) = \sum_n \frac{\nu_N}{N!} \tau^N = -\tau + \frac{12}{14} \tau^2 - \frac{29}{42} \tau^3 + \frac{79}{147} \tau^4 - \frac{2085}{5096} \tau^5 + \dots \quad (22)$$

Next, using Eq.(20), the one-point cumulants in 2D (Munshi et al. 1999), denoted as  $\Sigma_N$  as opposed to  $S_N$  parameters which represent the cumulants in 3D, can be used to compute the cumulants to arbitrary order in 2D (Munshi et al. 1999).

$$\Sigma_3 = \frac{36}{7}; \quad \Sigma_4 = \frac{2540}{49}; \quad \Sigma_5 = 793; \quad \Sigma_6 = 16370; \quad (23)$$

The generalization of the one-point cumulants i.e the  $S_N$  parameters to the two-point cumulant correlators  $C_{pq} = \langle \delta_1^p \delta_2^q \rangle_c / \langle \delta^2 \rangle_c^{p+q-1} \langle \delta_1 \delta_2 \rangle_c$  or  $C_{pq}$  parameters was introduced in (Bernardeau 1996). The lower-order normalized cumulant correlators can also be expressed in terms of the tree-level vertices  $\nu_N$  just as the one-point cumulants introduced in Eq.(20).

$$C_{21} = 2\nu_2; \quad C_{31} = 3\nu_3 + 6\nu_2^2; \quad C_{41} = 4\nu_4 + 36\nu_3\nu_2 + 24\nu_2^3. \quad (24)$$

To compare with observed or simulated data smoothing of the field is necessary. The smoothed generating function  $\mathcal{G}_{\delta}^s$  can be computed from the unsmoothed generating function  $\mathcal{G}_{\delta}$ . The generating functions  $\mathcal{G}_{\delta}^s$  and  $\mathcal{G}_{\delta}$  are related by the following implicit relation

(Bernardeau 1995)

$$\mathcal{G}_\delta^s(\tau) = \mathcal{G}_\delta(\tau[1 + \mathcal{G}_\delta^s]^{-(2+n)/4}). \quad (25)$$

A *tophat* smoothing window is assumed and the power spectrum is approximated locally as a power law  $P(k) \propto k^n$  (Munshi et al. 1999; Bernardeau 1995). For other window functions, e.g. Gaussian window generic results are not possible for arbitrary  $N$ . However, an order-by-order approach can be adopted to obtain the lower-order cumulants (Matsubara 2012). Notice that the smoothed power law depends on the spectral index while unsmoothed vertices depend solely on the gravitational collapse in 3D spherical or cylindrical in 2D. The smoothed vertices can be recovered by Taylor-expanding the smoothed generating function  $\mathcal{G}^s$ . Using these vertices it is possible to now compute the 2D skewness  $\Sigma_3$  and kurtosis  $\Sigma_4$  can be computed (Munshi et al. 1999):

$$\Sigma_3 = \frac{36}{7} - \frac{3}{2}(n+2); \quad (26a)$$

$$\Sigma_4 = \frac{2540}{49} - 33(n+2) + \frac{21}{4}(n+2)^2. \quad (26b)$$

These expressions are derived using 2D where gravitational collapse with cylindrical symmetry is relevant as is the case for projected surveys. However, the underlying statistics for the 3D density field is linked to spherical collapse which we have not considered here but may be relevant for a 3D weak lensing scenario where photometric data is used. However, there is a crucial difference between 2D and 3D statistics. For large separations in 3D we can factorise  $C_{pq} = C_{p1}C_{q1}$ , while in 2D this approximation is not valid. Thus, we will consider the family of statistics  $C_{p1}$  for arbitrary  $p$ .

$$\mathcal{S}_\ell^{(21)} = R_2 \Sigma_{21} P^\kappa(l) \sigma_L^2 = R_2 \left[ \frac{24}{7} - \frac{1}{2}(n+2) \right] P_\delta(l) \sigma_L^2; \quad \sigma_L^2 = \langle \kappa^2 \rangle; \quad (27a)$$

$$R_2 = \int_0^{r_s} dr \frac{w^3(r)}{d_A^{4+2n}(r)} \bigg/ \left( \int_0^{r_s} dr \frac{w^2(r)}{d_A^{2+n}(r)} \right)^2. \quad (27b)$$

The corresponding result at the fourth-order is given by:

$$\mathcal{K}_\ell^{(31)} = R_3 \Sigma_{31} P^\kappa(l) \sigma_L^4 = R_3 \left[ \frac{1473}{49} - \frac{195}{14}(n+2) + \frac{3}{2}(n+2)^2 \right] P_\delta(l) \sigma_L^4; \quad (28a)$$

$$R_3 = \int_0^{r_s} dr \frac{w^4(r)}{d_A^{6+3n}(r)} \bigg/ \left( \int_0^{r_s} dr \frac{w^2(r)}{d_A^{2+n}(r)} \right)^3. \quad (28b)$$

The dynamical contribution is encoded on  $\Sigma_{p1}$  where as the line-of-sight integration is represented by the pre-factors in  $R_p$ .

Historically the generating function approach was developed without any reference to perturbative dynamics and the vertices were left undetermined. Many generic predictions were developed coupling scaling Ansätze with the generating function formalism (Balian & Schaeffer 1989). While in the quasi-linear regime the loop corrections to the tree-level results violate the scaling Ansatz, in the highly nonlinear regime the vertices are known to become shape independent parameter as encapsulated in Hyper Extended Perturbation Theory (Scoccimarro & Frieman 2012). In recent years some of the results were derived the Large Deviation Principle (Bernardeau & Reimberg 2016; Uhlemann et al. 2016; Reimberg & Bernardeau 2018; Uhlemann et al. 2018).

Previously, many studies have focused on observed and simulated data of one-point cumulants (Bernardeau 1995; Munshi, Coles & Melott 1989) as well as for the two-point cumulant correlators (Munshi, Coles & Melott 1989; Bernardeau 1995). Previous studies have focused on galaxy surveys. In this paper we extend these results to the context of weak lensing.

## 6 HIGHER-ORDER SPECTRA IN THREE DIMENSIONS

Next, we will consider higher-order statistics in three dimensions (3D). Future surveys such as Euclid will go beyond the projection and using photometric redshifts will be able to retain radial information. In 3D we will compute the higher-order spectra as before in the low- $\ell$  limit. The results have similar characteristics as in projection, which we have discussed in §5 but are very different in certain aspect as we discuss below. We will decompose the lensing field in two different eigenmodes (a) Fourier-Bessel decomposition typically used for radially symmetric fields and (b) The generic Fourier-Cartesian decomposition that are most commonly used for perturbative analysis.



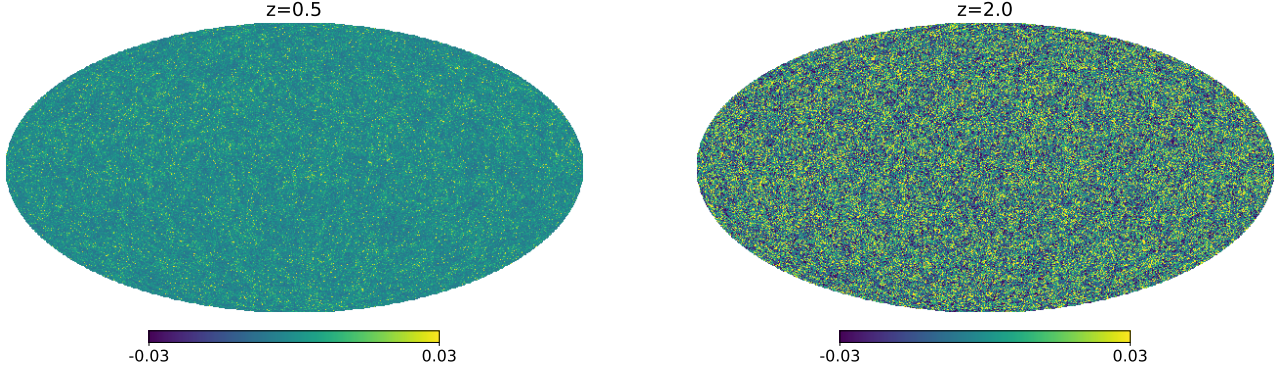


**Figure 1.** Examples of simulated  $\kappa$  maps used in our study. The left panel corresponds to  $z_s = 0.5$  while the right panel corresponds to  $z_s = 2.0$ . The maps were generated at a resolution of  $N_{\text{side}} = 4096$ . See §8 for more detail discussion about construction of maps used in our study.

We will use follow the same convention for forward and reverse Fourier transformation introduced in Eq.(2) for the Cartesian co-ordinate. For an arbitrary function  $A(\mathbf{r})$  with  $\mathbf{r} \equiv (r, \hat{\Omega}) = (r, \theta, \phi)$  and its Fourier transform  $A(\mathbf{k}; r)$  we will use:

$$A(\mathbf{r}; r) = \int d\mathbf{k} A(\mathbf{k}; r) \exp(i\mathbf{k} \cdot \mathbf{r}); \quad A(\mathbf{k}; r) = \int d\mathbf{r} A(\mathbf{r}; r) \exp(i\mathbf{k} \cdot \mathbf{r}). \quad (29)$$

In spherical-Bessel coordinates the eigenfunctions of the Laplacian operators are the products of spherical harmonics  $Y_{\ell m}(\hat{\Omega})$  and spherical Bessels function  $j_\ell(r)$  i.e.  $j_\ell(kr)Y_{\ell m}(\hat{\Omega})$  the transforms take the following form:

$$A_{\ell m}(k) \equiv \sqrt{\frac{2}{\pi}} \int d^3\mathbf{r} A(\mathbf{r}) k j_\ell(kr) Y_{\ell m}^*(\hat{\Omega}); \quad A(\mathbf{r}) \equiv \sqrt{\frac{2}{\pi}} \int k dk \sum_{\ell=0}^{\infty} \sum_{m=-\ell}^{\ell} A_{\ell m}(k) j_\ell(kr) Y_{\ell m}(\hat{\Omega}). \quad (30)$$

Using the well-known Rayleigh expansion that expands the plane-wave in a spherical wave basis:

$$\exp(i\mathbf{k} \cdot \mathbf{r}) = 4\pi \sum_{\ell} \sum_{m=-\ell}^{m=\ell} i^\ell j_\ell(kr) Y_{\ell m}(\hat{\Omega}_k) Y_{\ell m}(\hat{\Omega}); \quad \hat{\Omega}_k = (\theta_k, \phi_k). \quad (31)$$

we can relate the spherical harmonic coefficients  $A_{\ell m}$  with their Fourier counterpart  $A$ :

$$A_{\ell m}(k; r) = \frac{1}{(2\pi)^{3/2}} k i^\ell \int d\hat{\Omega}_k A(\mathbf{k}; r) Y_{\ell m}(\hat{\Omega}_k). \quad (32)$$

The 3D power spectrum  $P^{\text{AA}}(k)$  defined respectively in Cartesian coordinates and  $\mathcal{C}_\ell^{\text{AA}}$  in spherical coordinates are:

$$\langle A(\mathbf{k}) A^*(\mathbf{k}) \rangle = (2\pi)^3 P^{\text{AA}}(k); \quad \langle A_{\ell m}(k, l) A_{\ell' m'}^*(k') \rangle = (2\pi)^2 \mathcal{C}_\ell^{\text{AA}}(k; r) \delta_{1D}(k - k') \delta_{\ell\ell'} \delta_{mm'}. \quad (33)$$

In general, in the absence of any mask, it can be shown that:  $\mathcal{C}_\ell = P(k)$  i.e. the 3D power spectrum in spherical co-ordinate is independent of  $\ell$  and is actually same as the power spectrum in Cartesian co-ordinates (Castro, Heavens, Kitching 2005). Next, for the construction of the higher-order 3D spectra we will define the following cross-spectra between two arbitrary 3D fields  $A(\mathbf{r})$  and  $B(\mathbf{r})$  in spherical co-ordinates:

$$\langle A(\mathbf{k}) B^*(\mathbf{k}) \rangle = (2\pi)^3 P^{\text{AB}}(k); \quad \langle A_{\ell m}(k; r) B_{\ell' m'}^*(k'; r) \rangle = (2\pi)^2 \mathcal{C}_\ell^{\text{AB}}(k; r) \delta_{1D}(k - k') \delta_{\ell\ell'} \delta_{mm'}. \quad (34)$$

Using this identity, for the 3D density field  $\delta$  we can derive the following expressions for the higher-order spectra of the density field:

$$P^\delta(k; r, r') = \langle \delta(\mathbf{k}; r) \delta^*(\mathbf{k}', r') \rangle_c; \quad \mathcal{C}_\ell^\delta(k; r, r') = \langle \delta_{\ell m}(k; r) \delta_{\ell m}^*(k; r') \rangle_c; \quad P^\delta(k; r, r') = \mathcal{C}_\ell^\delta(k; r, r'). \quad (35a)$$

$$S^{21, \delta}(k; r, r') = \langle \delta^2(\mathbf{k}; r) \delta^*(\mathbf{k}'; r') \rangle_c; \quad S_\ell^{21, \delta}(k; r, r') = \langle \delta_{\ell m}^2(k; r) \delta_{\ell m}^*(k; r') \rangle_c; \quad S^{21, \delta}(k, r, r') = S_\ell^{21, \delta}(k; r, r'). \quad (35b)$$

$$T^{31, \delta}(k; r, r') = \langle \delta^3(\mathbf{k}; r) \delta^*(\mathbf{k}'; r') \rangle_c; \quad T_\ell^{31, \delta}(k, r) = \langle \delta_{\ell m}^2(k; r) \delta_{\ell m}^*(k; r') \rangle_c; \quad T^{31, \delta}(k, r, r') = T_\ell^{31, \delta}(k, r, r'). \quad (35c)$$

$$T^{22, \delta}(k, r, r') = \langle \delta^2(\mathbf{k}; r) \delta^{2*}(\mathbf{k}'; r') \rangle_c; \quad T_\ell^{22, \delta}(k; r, r') = \langle \delta_{\ell m}^2(k; r) \delta_{\ell m}^{2*}(k; r') \rangle_c; \quad T^{22, \delta}(k, r, r') = T_\ell^{22, \delta}(k; r, r'). \quad (35d)$$

In our notation,  $\delta^p(k)$  is the Fourier transform of  $\delta^p$ . Notice these expressions are non-perturbative and are valid irrespective of detailed modelling and are valid to an arbitrary order i.e. when cross-correlating p-th power of  $\delta$  against the q-th power i.e. in  $\langle \delta^p(\mathbf{k}) \delta^q(\mathbf{k}) \rangle$  in spherical or Cartesian co-ordinate. In the Cartesian co-ordinate the normalized cumulant correlators  $C_{pq}$  are defined as follows:

$$\langle \delta^p(\mathbf{k}) \delta^{q*}(\mathbf{k}) \rangle_c = C_{pq} \langle \delta^2 \rangle_c^{p+q-2} P(k) = C_{pq} \langle \delta^2 \rangle_c^{p+q-2} \mathcal{C}_\ell(k) \quad (36)$$

The second step relies on Eq.(35a). In the real-space Eq.(36) this is equivalent to:

$$\langle \delta^p(\mathbf{r}_1) \delta^{q*}(\mathbf{r}_2) \rangle_c = C_{pq} \langle \delta^2 \rangle_c^{p+q-2} \langle \delta(\mathbf{r}_1) \delta(\mathbf{r}_2) \rangle_c. \quad (37)$$

The results Eq.(35a) - Eq.(35d) are non-perturbative and do not depend on any simplifying assumptions. However, in case of studies of galaxy clustering it is more natural to study high-order statistics in the redshift space. Similarly, for 3D weak lensing, line-of-sight integration will need to be taken into account. Such extensions will be presented separately. The coefficients  $C_{pq}$  defined in Eq.(36) can be computed using perturbative calculations. In 3D the smoothed and unsmoothed vertex generating functions are related through an implicit expression (Bernardeau 1996) which is analogous to Eq.(25).

$$\mathcal{G}_\delta^s(\tau) = \frac{3}{2} \mathcal{G}_\delta(\tau [1 + \mathcal{G}_\delta^s]^{-(3+n)/6}). \quad (38)$$

The power spectrum is assumed to be approximated locally by a power law with power law index  $n$  i.e.  $P(k) \propto k^n$ . On Taylor expanding the 3D (unsmoothed) generating function  $\mathcal{G}(\tau)$ , we can recover the lower order vertices  $\nu_N$  in 3D (Bernardeau et al. 2002):

$$\mathcal{G}_\delta(\tau) = \sum_n \frac{\nu_N}{N!} \tau^N = -\tau + \frac{34}{21} \tau^2 - \frac{682}{189} \tau^3 + \dots \quad (39)$$

Using these vertices it is possible to compute the normalized lower-order moments i.e. skewness  $S_3$  and kurtosis  $S_4$  in 3D (Bernardeau et al. 2002):

$$S_3 = \frac{34}{7} - (n+3); \quad S_4 = \frac{60712}{1323} - \frac{62}{3}(n+3) + \frac{7}{3}(n+3)^3. \quad (40a)$$

The lower-order cumulant correlators have the following form (Bernardeau et al. 2002):

$$C_{21} = \frac{68}{21} - \frac{(n+3)}{3}; \quad C_{31} = \frac{11710}{441} - \frac{61}{7}(n+3) + \frac{2}{3}(n+3)^3. \quad (40b)$$

Detailed derivations regarding construction of one- and two-point probability distribution functions are detailed in (Bernardeau et al. 2002). The 3D vertices defined in Eq.(39) assume a different numerical value though the formal structure remains the same. In addition a more generic results  $C_{pq} = C_{p1} C_{q1}$  gives a much needed consistency check. The results in a 3D collapse are related to a spherical window and the dynamics relate to the 3D spherical collapse.

## 7 PSEUDO- $\mathcal{C}_\ell$ (PCL) ESTIMATORS

Maximum likelihood (ML) estimators or quadratic maximum likelihood (QML) estimators are most obvious choices for analyzing cosmological data sets. However, these estimators require inverse covariance weighting which clearly is not practical for large cosmological data sets though various clever algorithmic techniques have been considered (Bernardeau et al. 2002). This has resulted in the development of many sub-optimal estimators which uses heuristic weighting schemes. The so-called pseudo- $\mathcal{C}_\ell$  (PCL) technique was introduced in (Hivon et al. 2012); see Szapudi et al. (2012) for a related method. These estimators are unbiased but sub-optimal. Various weighting schemes depending on sky coverage as well as noise characteristic as well as various hybridization schemes to combine large angular

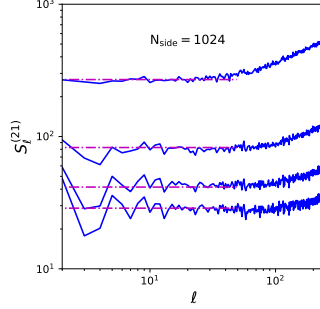


**Figure 2.** The skew-spectrum  $S_{\ell}^{(21)}$  defined in Eq.(10a)-Eq.(10b) is shown as a function of the harmonics  $\ell$ . From top to bottom the curves correspond to source redshifts  $z_s = 0.5, 1.0, 1.5$  and  $2.0$  respectively. A total of 10 simulations were used to compute the  $S_{\ell}^{(21)}$ . The straight lines at the left correspond to predictions from perturbation theory encapsulated in Eq.(27a)- Eq.(27b). We have assumed a power-law power spectrum  $P_{\delta}(k) \propto k^n$ . We have chosen  $n = -2.0$  (dot-dashed lines). See text for details.

scale (equivalently the low  $\ell$ ) estimates using QML with small angular scale (high  $\ell$ ) PCL estimates. were considered in (Efstathiou 2004).

$$M_{\ell\ell'} = (2\ell' + 1) \sum_{\ell''} \begin{pmatrix} \ell & \ell' & \ell'' \\ 0 & 0 & 0 \end{pmatrix}^2 \frac{(2\ell'' + 1)}{4\pi} |w_{\ell''}|^2; \quad (41a)$$

$$\hat{S}_{\ell}^{(21)} = \sum_{\ell'} M_{\ell\ell'}^{-1} \tilde{S}_{\ell'}^{(21)}. \quad (41b)$$

Here  $\tilde{S}_{\ell'}^{(21)}$  denotes the skew-spectrum computed from a map in the presence of a mask  $w(\hat{\Omega})$ ,  $\hat{S}_{\ell'}^{(21)}$  is the all-sky estimate and  $w_{\ell} = 1/(2\ell + 1) \sum_m w_{\ell m} w_{\ell m}^*$  is the power spectrum of the mask constructed from the harmonic-coefficient  $w_{\ell m}$  of the map. The coupling matrix  $M_{\ell\ell'}$  represents the mode-mixing due to the presence of a mask. The generalization of the PCL method to estimate higher-order spectra were developed in (Munshi et al. 2011a,b) for spin-0 fields and in higher spin fields in (Munshi et al. 2012) as well as in 3D in (Munshi et al. 2011). Exactly same result holds for higher-order spectra, e.g., for all-sky estimate of kurt-spectrum  $\hat{\mathcal{K}}_{\ell}^{(21)}$  and its masked counterpart  $\tilde{\mathcal{K}}_{\ell'}^{(21)}$  are related through a similar expression  $\hat{\mathcal{K}}_{\ell}^{(31)} = \sum_{\ell'} M_{\ell\ell'}^{-1} \tilde{\mathcal{K}}_{\ell'}^{(31)}$ . This has also been generalized to reconstruct the Minkowski Functionals in an order-by-order manner (Munshi et al. 2012,?) Two equivalent techniques for flat-sky PCLs are developed here (Asgari et al. 2012) and (Hikage et al. 2012).

## 8 NUMERICAL SIMULATIONS

We use the publicly available all-sky weak-lensing maps generated by (Takahashi et al. 2012)<sup>10</sup> that were generated using ray-tracing through N-body simulations. Multiple lens planes were used to generate convergence ( $\kappa$ ) as well as shear ( $\gamma$ ) maps. Many recent studies were performed using these maps, e.g. Namikawa et al. (2018); Munshi et al. (2019a). In these simulations, the source redshifts used were in the range  $z_s = 0.05 - 5.30$  at interval  $\Delta z_s = 0.05$ . In this study, we have used the maps with  $z_s = 0.5, 1.0, 1.5, 2.0$ . The maps do include post-Born corrections (Lewis & Pratten 2016). Though at the low source redshift such corrections only play a negligible role. Indeed, they do play significant role in CMB lensing. The convergence maps were generated using an equal area pixelisation scheme, in HEALPIX<sup>11</sup> format (Gorski et al. 2016). In this pixelisation scheme the number of pixels scale as  $N_{\text{pix}} = 12N_{\text{side}}^2$  where  $N_{\text{side}}$  is the resolution parameter which can take values  $N_{\text{side}} = 2^N$  with  $N = 1, 2, \dots$ . The set of maps we use are generated at  $N_{\text{side}} = 4096$

<sup>10</sup> [http://cosmo.phys.hirosaki-u.ac.jp/takahashi/allsky\\_raytracing/](http://cosmo.phys.hirosaki-u.ac.jp/takahashi/allsky_raytracing/)

<sup>11</sup> <https://healpix.jpl.nasa.gov/>

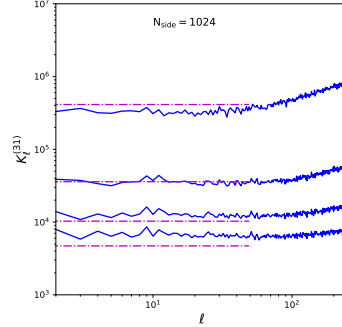


**Figure 3.** The skew-spectrum  $K_\ell^{(31)}$  defined in Eq.(15a) is shown as a function of the harmonics  $\ell$ . From top to bottom the curves correspond to source redshifts  $z_s = 0.5, 1.0, 1.5$  and  $2.0$  respectively. A total of 10 simulations were used to compute the  $K_\ell^{(31)}$ . The straight lines at the left correspond to predictions from perturbation theory encapsulated in Eq.(28a)-Eq.(28b). We have assumed a power-law power spectrum  $P_\delta(k) \propto k^n$ . We have chosen  $n = -2$ . See text for details.

which were also cross-checked using higher resolution maps that were constructed at a resolution  $N_{\text{side}} = 8192, 16384$ . These maps were found to be consistent with each other up to the angular harmonics  $\ell \leq 3600$ . In addition detailed tests were performed by using a Electric/Magnetic (E/B) decomposition of shear maps for the construction of  $\kappa$  maps (Takahashi et al. 2012). Though we have used high resolution maps  $N_{\text{side}} = 4096$ , we have degraded them to low resolution maps at  $N_{\text{side}} = 1024$  as we are primarily interested in the perturbative regime. The following set of cosmological parameters  $\Omega_{\text{CDM}} = 0.233$ ,  $\Omega_b = 0.046$ ,  $\Omega_M = \Omega_{\text{CDM}} + \Omega_b$ ,  $\Omega_\Lambda = 1 - \Omega_M$  and  $h = 0.7$  were used to generate the maps assuming a  $\Lambda$ CDM background cosmology. The amplitude of density fluctuations  $\sigma_8 = 0.82$  and the spectral index  $n_s = 0.97$ . Examples of  $\kappa$  maps used in our study are presented in Figure-1. We will focus on the large-separation or the small  $\ell$  regime in our study and we do not expect the baryonic feedback to play a significant role (Weiss et al. 2019). It is worth mentioning here that these maps were also used to recently analyze the bispectrum in the context of CMB lensing (Namikawa et al. 2018).

## 9 TESTS AGAINST NUMERICAL SIMULATIONS

The skew-spectrum  $\mathcal{S}_\ell^{(21)}$  is shown as a function of the harmonics  $\ell$  in Figure-2. From top to bottom the curves represent the source redshifts  $z_s = 0.5, 1.0, 1.5$  and  $2.0$  respectively. The results are from maps with  $N_{\text{side}} = 1024$ . We have analyzed these maps for  $\ell_{\text{max}} = 2N_{\text{side}}$ . The straight lines correspond to perturbative results computed using tree-level perturbation theory Eq.(27a) - Eq.(27b). We have used an ensemble of ten realisations to compute the mean which is being plotted. We use all-sky maps without an observational mask. The effect of mask can be incorporated using Eq.(41a)-Eq.(41b).

The  $\mathcal{K}_\ell^{(31)}$  is shown as a function of the harmonics  $\ell$  in Figure-3. From top to bottom the curves represent the source redshifts  $z_s = 0.5, 1.0, 1.5$  and  $2.0$  respectively. The maps used are  $N_{\text{side}} = 1024$  and as before we have analyzed for  $\ell_{\text{max}} = 2N_{\text{side}}$ . The straight lines correspond to perturbative results computed using tree-level perturbation theory Eq.(28a) - Eq.(28b). We have used an ensemble of ten realisations to compute the mean which is being plotted. We use all-sky maps without an observational mask.

Our results for the skew- and kurt-spectra are derived in the large separation limit i.e. the cumulant correlators defined, e.g. in Eq.(12) and in Eq.(19b)  $|\xi_{12}|/\bar{\xi}_2 \ll 1$ . In real-space this limit was seen to be reached very fast as soon as the two neighboring cells are not overlapping. In harmonic domain the scale  $\ell$  represents the separation of two beam-smoothed pixels for which the skew-spectrum is being measured. Thus, large separation in our case corresponds to low  $\ell$ , and typical size of the pixels corresponds to the  $\ell$  at which the beam can no longer be approximated as unity. This is the scale where the correction to the skew-spectrum starts to be non-negligible. These corrections, which are of order  $\xi_{ij}/\bar{\xi}_2 \ll 1$ , are difficult to compute analytically. Though, entire skew-spectrum can be computed with fitting functions. Clearly, such a computation will not be possible beyond third-order i.e. skew-spectrum due to lack of such a fitting function at the fourth-order. Thus, the techniques developed here are valuable as their predictions can be made at *all-orders*.

The results we have computed are based on spherical top-hat window. However, many previous studies have shown that the actual shape of the window is not important, and replacing the circle with square can be a very good approximation (Munshi et al. 1999).

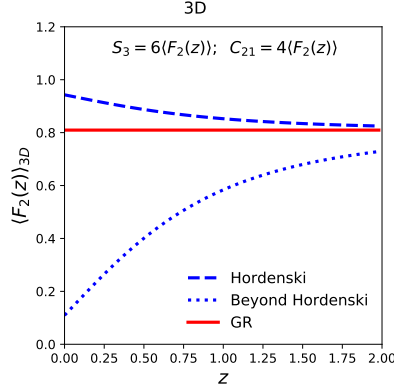


**Figure 4.** The second-order tree-level perturbative vertex  $\langle F_2(z) \rangle_{3D}$  is plotted as a function of redshift  $z$  for 3D surveys as given in Eq.(48). Three different cases shown correspond to the Horndeski, Beyond Horndeski and GR as indicated. See text for more details. The results are shown for unsmoothed field i.e.  $n = -3$ . We have used the parameterizations in Eq.(66b) for various models. The Horndeski model is given by  $\xi_\kappa = 1, \xi_\lambda = 0$  and the beyond Horndeski theories are given by  $\xi_\kappa = 1, \xi_\lambda = 1$ . For the GR we have  $\xi_\kappa = 0, \xi_\lambda = 0$ .

However, profile of the smoothing beam or window as opposed to its shape can change the theoretical predictions. The predictions for a Gaussian window was worked out in detail in (Matsubara 2012). However, results can be derived only in order-by-order manner and approaches based on generating functions are not applicable.

A few comments about going beyond kurt-spectrum are in order. Extraction and interpretation of higher-order statistics can be rather complex from any cosmological data-sets. Estimators of the cumulants and cumulant correlators are typically known to be biased and elaborate scheme were developed in estimating and correcting such bias as well as scatter in estimators typically used for evaluating these quantities mainly in real space in the context of galaxy clustering. Such corrections are expected to be more dominant role with increasingly higher-order (Munshi et al. 1999). Such corrections and their accurate calibration against simulations are lacking in the literature. Though, for lower-order statistics we probed here, such corrections are expected to be negligible, a better understanding of such effects is needed before we can interpret the statistics beyond kurt-spectra (equivalently trispectrum).

An alternative approach considered by various authors was to consider the one-point and two-point probability functions which encode cumulants and their correlators to an arbitrary order (Munshi & Jain 2000; Munshi 2000). These results are applicable in real-space which make them useful for surveys with low-sky coverage. The results derived here will be relevant for surveys with high sky-coverage where harmonics decomposition would mean less correlated measurements for individual  $\ell$ .

By their very nature, projected or 2D surveys unlike their 3D counterparts mixes scale which makes assigning exact spectral index with an angular scales or in our case the harmonic  $\ell$ . We have shown how much variation we should expect for a range of feasible spectral index  $n$ . Finally, the redshift dependence of the skew- and kurt-spectra is encoded in the coefficients  $R_2$  and  $R_3$ . It is however important to point out that these pre-factors are rather sensitive to the lower limit of the integration  $z_{\min}$  i.e. in Eq.(27b) and Eq.(27b). Numerical implementation of simulation of ray-tracing to generate convergence maps may introduce slight modification in  $z_{\min}$  which may lead to a bias in the theoretical predictions.

The excellent match between the theoretical predictions and simulations we have found here is encouraging for computing such corrections.

## 10 MODIFIED THEORIES OF GRAVITY: COMPUTATION OF $C_{21}$

The theoretical modelling of the bispectrum in modified gravity scenarios is more challenging than the power spectrum calculation. Typically a perturbative approach is adopted in the quasilinear regime (Bernardeau & Brax 2011). In addition, a quasi-static approximation is used, i.e. metric perturbations are varying slowly with time that they can be ignored. Many extensions of the perturbative approach

were considered in the literature in recent years (Bose & Taruya 2018; Namikawa, Bouchet & Taruya 2018). Typically, this is achieved by introducing more freedom to the kernels and validating or calibrating them using numerical simulations. Indeed, others including variants of halo model predictions too have been proposed that can reproduce the simulation results with varying degree of success.

In the literature, typically, two main families of modified gravity theories are considered. (A) models with Vainshtein-screening mechanism which includes the DGP model as well as the Horndeski (Horndeski 1974) and beyond Horndeski theories (Gleyzes et al. 2015a,b; Langois & Noui 2016) and (B) the models with Chameleon-screening that includes the Hu-Sawicki  $f(R)$  model (Hu & Sawicki 2016). In the DGP model (Dvali, Gabadadze, Porati 2000) the bispectrum from simulations can be reproduced using the GR expression by suitably modifying the power spectrum. The situation is somewhat more complicated for  $f(R)$  theories. The numerical modelling is more important at small scales where analytical results start to fail.

### 10.1 Bernardeau & Brax Models

Next, we first turn to different phenomenological toy models of modified gravity presented by Bernardeau & Brax (2011).

**(a) Gamma  $\gamma$  Model:** This model is generated by modifying the Euler equation of the Euler-Continuity-Poisson equation. In this model the gravitational field seen by massive particles (denoted as  $\phi^{\text{eff}}$ ) is different from the gravitational potential that solved the Poisson equation  $\phi$ . These two potentials are different and related by  $\phi^{\text{eff}} = (1 + \epsilon)\phi$  through parameter  $\epsilon(t)$  in the sub-horizon scale.

In this parametrization the kernel  $F_2$  in Eq.(1b) is modified to the following form:

$$F_2(\mathbf{k}_1, \mathbf{k}_2) = \frac{1}{2}(1 + \epsilon) + \frac{1}{2} \frac{\mathbf{k}_1 \cdot \mathbf{k}_2}{k_1 k_2} \left( \frac{k_1}{k_2} + \frac{k_2}{k_1} \right) + \frac{1}{2}(1 - \epsilon) \left[ \frac{\mathbf{k}_1 \cdot \mathbf{k}_2}{k_1 k_2} \right]^2 \quad (42)$$

In general the parameter  $\epsilon$  can be a function of scale factor  $a$  or the wavelength  $k$ . For  $\epsilon = 3/7$  recover the expression given in Eq.(1c). The Lagrangian perturbation theory is often used to model quasilinear evolution of gravitational clustering. The Zel'dovich approximation is the linear order in Lagrangian perturbation theory. The bispectrum in the Zel'dovich approximation can be recovered from Eq.(42)  $\epsilon = 0$  (Munshi, Sahni, Starobinsky 1994).

$$\langle F_2 \rangle_{3D} = \frac{\epsilon + 2}{3}; \quad \langle F_2 \rangle_{2D} = \frac{\epsilon + 3}{4}. \quad (43)$$

The actual value of the parameter  $\epsilon$  can be computed using the linearised Euler-Continuity-Poisson equation, and assuming a parametric form for the growth factor  $f = d \ln D_+ / d \ln a \approx \Omega_M^{-1/2}$ . A convenient form of a fitting function can be obtained for values not too far from General Relativistic ( $\Lambda$ CDM) values. This model can be considered as a special case of Eq.(66b) with  $\kappa = 1$  and  $\epsilon = 1 - 4/7\lambda$ . The smoothing includes a dependence on spectral index. In 2D we have

$$C_{21} = R_2 \left[ 4 \langle F_2 \rangle_{2D} - \frac{1}{2}(n + 2) \right]. \quad (44)$$

**(b) Beta ( $\beta$ ) Model:** In the  $\beta$  model proposed by (Bernardeau & Brax 2011) where the expression for the kernel  $F_2(\mathbf{k}_1, \mathbf{k}_2)$  we have:

$$F_2(\mathbf{k}_1, \mathbf{k}_2) = \left( \frac{3\nu_s}{4} - \frac{1}{2} \right) + \frac{1}{2} \frac{\mathbf{k}_1 \cdot \mathbf{k}_2}{k_1 k_2} \left[ \frac{k_1}{k_2} + \frac{k_2}{k_1} \right] + \left( \frac{3}{2} - \frac{3\nu_s}{2} \right) \left[ \frac{\mathbf{k}_1 \cdot \mathbf{k}_2}{k_1 k_2} \right]^2 \quad (45)$$

where, the parameter  $\nu_2$  can be related to the  $\epsilon$  parameter in Eq.(42)  $\epsilon = \frac{3}{2}\nu_s - 2$ . The parametric value for  $\nu_2$  can be obtained in a manner similar to the  $\gamma$  model. However, we would leave them unspecified. The angular average gives  $\langle F_2 \rangle_{3D} = \nu_s/2$  and similarly  $\langle F_2 \rangle_{2D} = (3\nu_s/2 + 1)/4$  for 2D and is independent of  $t$ . In these models the  $\nu_2$  can in general be a function of  $z$  as well as wave-number  $k$ . This model was also recently used in (Munshi 2017) for computation of a related statistics known as integrated bispectrum. In general the parameter can also be a  $k$  dependent parameter. The expression for  $C_{21}$  has the following form:

$$C_{21} = R_2 \left[ \frac{3}{2}\nu_s + 1 - \frac{1}{2}(n + 2) \right]. \quad (46)$$

The power spectrum too gets modified due to changes in the kernel  $F_2(\mathbf{k}_1, \mathbf{k}_2)$  at one-loop. The loop corrections to the linear power spectrum depends on the  $F_2(\mathbf{k}_1, \mathbf{k}_2)$  and thus can also be used to constrain any departure from GR.

## 10.2 Horndeski and Beyond Horndeski in the Perturbative Regime

Horndeski theories are scalar-tensor theories with a single propagating degree of freedom and are free from Ostrogradsky type instabilities. Horndeski theories have also been extended by considering what are also known as the degenerate higher-order scalar-tensor (DHOST) theories. The simplest extensions in the context of non-degenerate scenarios are also known as the Galezys-Langlois-Piazza-Venizzi or GPLV theories (Gleyzes et al. 2015a,b). The second-order kernel in these scenario include a scale dependent additional term which changes the bispectrum (Hirano, Kobayashi, Tashiro, Yokoyama 2017) that can be constrained using the staistics discussed here.

$$F_2(\mathbf{k}_1, \mathbf{k}_2, z) = \kappa_s(z)\alpha_s(\mathbf{k}_1, \mathbf{k}_2) - \frac{2}{7}\lambda_s(z)\gamma(\mathbf{k}_1, \mathbf{k}_2); \quad (47a)$$

$$\alpha_s(\mathbf{k}_1, \mathbf{k}_2) = 1 + \frac{1}{2}(\mathbf{k}_1 \cdot \mathbf{k}_2) \frac{(k_1^2 + k_2^2)}{k_1^2 k_2^2}; \quad \gamma_s(\mathbf{k}_1, \mathbf{k}_2) = 1 - \frac{(\mathbf{k}_1 \cdot \mathbf{k}_2)^2}{k_1^2 k_2^2}. \quad (47b)$$

Taking angular averages we can see  $\alpha_s(\mathbf{k}_1, \mathbf{k}_2) = 1$  and  $\gamma(\mathbf{k}_1, \mathbf{k}_2) = 1/2$  which leads us respectively in 2D to:

$$\langle F_2 \rangle_{2D} = \kappa_s(z) - \frac{1}{7}\lambda_s(z); \quad \langle F_2 \rangle_{3D} = \kappa_s(z) - \frac{4}{21}\lambda_s(z). \quad (48)$$

Similar calculation in the Effective Field Theory (EFT) of dark energy framework can be found in (Cusina, Lewandowskyi, Vernizzi 2018)

$$C_{21} = 2 \int_0^{r_s} dr D_+^4(z) \frac{w^3(r)}{d_A^{4+2n}(r)} \left[ \kappa_s(z) - \frac{1}{7}\lambda_s(z) - \frac{1}{2}\kappa_s(z)(n+2) \right] \Bigg/ \left( \int_0^{r_s} dr D_+^2(z) \frac{w^2(r)}{d_A^{2+n}(r)} \right)^2. \quad (49)$$

In Crisostomi, Lewandoski, Vernizzi (2019) the following equivalent parameterization for the kernel  $F_2$  was introduced:

$$F_2(\mathbf{k}_1, \mathbf{k}_3) = A_\alpha(z)\alpha_s(\mathbf{k}_1, \mathbf{k}_2) + A_\gamma(z)\gamma(\mathbf{k}_1, \mathbf{k}_2). \quad (50)$$

In terms of the parameters  $A_\alpha(z)$  and  $A_\gamma(z)$

$$C_{21} = 2 \int_0^{r_s} dr D_+^4(z) \frac{w^3(r)}{d_A^{4+2n}(r)} \left[ A_\alpha(z) + \frac{1}{2}A_\gamma(z) - \frac{1}{2}A_\alpha(z)(n+2) \right] \Bigg/ \left( \int_0^{r_s} dr D_+^2(z) \frac{w^2(r)}{d_A^{2+n}(r)} \right)^2. \quad (51)$$

In general the parameters  $A_\alpha(z) = \kappa_s(z)$ ,  $A_\gamma(z) = -2/7\lambda(z)$  are time-dependent. For this model we have  $\langle F_2 \rangle_{3D} = A_\alpha + \frac{2}{3}A_\gamma$  and  $\langle F_2 \rangle_{2D} = A_\alpha + \frac{1}{2}A_\gamma$ . It is important to notice that these theories have an important difference with GR and Horndeski theories. The Horndeski theories are invariant under time-dependent spatial co-ordinate transformations. The form for the  $F_2$  kernels are fixed by existence of such symmetry. Many modified gravity theories fall under this category. In Beyond Horndeski theories, the fluid equations and the equations of gravity possess very different symmetry properties and have a kernel  $F_2$  that is structurally different. This is related to violation of these theories from the so-called consistency relation which are respected in GR (Peloso & Pietroni 2008). Future surveys such as the *Euclid* survey will be able to probe such theories beyond the consistency relations using the statistics developed here.

A detailed study for the skew-spectrum (Munshi & Heavens 2010) Minkowski functionals (Munshi et al. 2012) for these models and the integrated bispectrum (Munshi et al. 2019b) as well as the related consistency relations will be presented elsewhere (Munshi et al. 2020, in preparation).

## 10.3 Normal-branch of Dvali, Gabadadze, Porrati (nDGP) model

The normal branch of (Dvali, Gabadadze, Porati 2000) model known also as the nDGP is a prototypical example that involve Vainshtein screening. The model of bispectrum that is known to accurately reproduce the bispectrum was computed by (Koyama, Taruya, Hiramatsu 2009) which correspond to the case  $\kappa = 1$  in Eq.(66b).

$$\kappa_s(z) = 1; \quad \lambda_s(z) = \left( 1 - \frac{7}{2} \frac{D_2(z)}{D_+^2(z)} \right). \quad (52)$$

Here  $D_2(z)$  and  $D_+(z)$  are the first-order and second-order growth factors that can be computed by numerically solving the equations governing growth of perturbations (Bose & Taruya 2018).

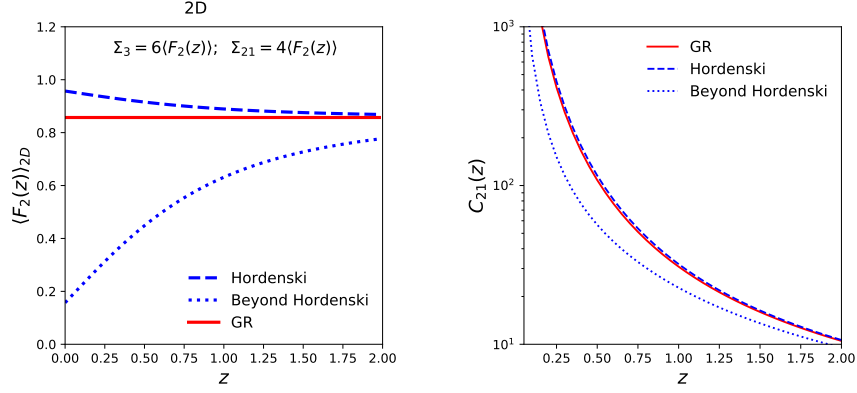


**Figure 5.** The left panel shows  $\langle F_2(z) \rangle_{2D}$  for GR, Horndeski and Beyond Horndeski as a function of redshift  $z$  in 2D. The results are plotted for  $n = -2$  which represents the unsmoothed field. The right panel corresponds to  $C_{21}(z)$  as a function for these models.

#### 10.4 Massive Neutrinos

A small but non-negligible fraction of the cosmological matter density is provided by massive neutrinos (Lesgourgues & Pastor 2006). The massive neutrinos are known to have significant thermal distribution and a different cosmological evolutionary history in comparison to the cold dark matter. The thermal dispersion in velocity results in a damping of perturbation below a length scale also known as the free-streaming length scale. This will be probed by future surveys with a very high degree of accuracy. In the long run cosmological surveys are expected to provide an upper limit to the sum of the neutrino masses.. This will be very useful when jointly considered with the lower limits from neutrino-oscillation experiments.

The neutrinos decouple and free-stream with a large thermal velocities. The redshift  $z_{nr}$  at which neutrinos become relativistic depend on their mass eigenstate  $m_i$ ,  $1 + z_{nr} = 1980 [m_{\nu,i}/1\text{eV}]$  The fractional contribution to the total matter density is denoted as  $f_\nu$  which can be expressed as

$$f_\nu \equiv \frac{\Omega_\nu}{\Omega_M} = \frac{1}{\Omega_{M,0} h^2} \frac{\sum_i M_{\nu,i}}{93.14\text{eV}}. \quad (53)$$

In future it will also be interesting to consider the effect of neutrino mass on bispectrum when simulated all-sky lensing maps for such cosmologies will be available (Liu et al. 2018; Coulton et al. 2018). The total matter distribution thus can be written in terms of the cold dark matter perturbation  $\delta_{cdm}$  and the fluctuations in the neutrino density distribution  $\delta_\nu$ .

$$\delta_m = f_c \delta_c + f_\nu \delta_\nu; \quad f_c + f_\nu = 1. \quad (54)$$

The resulting matter power spectrum  $P_{mm}(k)$  and bispectrum  $B_{mmm}(\mathbf{k}_1, \mathbf{k}_2, \mathbf{k}_3)$  can be expressed as (Ruggeri 2018):

$$P_{mm}(k) = f_c^2 P_{cc}(k) + 2f_\nu f_c P_{\nu c}(k) + f_\nu^2 P_{\nu\nu}(k) \quad (55a)$$

$$B_{mmm} = f_c^3 B_{ccc} + f_c^2 f_\nu B_{cc\nu} + f_c f_\nu^2 B_{\nu\nu c} + f_\nu^3 B_{\nu\nu\nu}. \quad (55b)$$

Here  $P_{cc}$  and  $P_{\nu\nu}$  represent the power spectrum cold dark matter and the neutrino component where as the  $P_{\nu c}$  is the cross spectra between them. We will drop the suffix 3D to avoid cluttering. We will only consider the linear order perturbation in  $\delta_\nu$  and ignore all higher order contributions which implies  $B_{\nu\nu\nu} = 0$ . For  $B_{ccc}$  the expression in the squeezed limit is exactly same as derived before.

$$B_{ccc}^{2D,sq} = \left[ \frac{24}{7} - \frac{1}{2} \frac{dk^2 P_{cc}(k)}{d \ln k} \right] P_{cc}(k_\perp) P_{cc}(q_{3\perp}). \quad (56a)$$



We will next consider the mixed terms  $B_{\nu\nu c}$ . These contributions in terms of  $\delta_c$  and  $\delta_\nu$  can be expressed as:

$$B_{cc\nu}(\mathbf{k}_1, \mathbf{k}_2, \mathbf{k}_3) = \langle \delta_c(\mathbf{k}_1) \delta_c(\mathbf{k}_2) \delta_\nu(\mathbf{k}_3) \rangle + \text{cyc.perm.}; \quad (57a)$$

$$B_{\nu\nu c}(\mathbf{k}_1, \mathbf{k}_2, \mathbf{k}_3) = \langle \delta_\nu(\mathbf{k}_1) \delta_\nu(\mathbf{k}_2) \delta_c(\mathbf{k}_3) \rangle + \text{cyc.perm.}. \quad (57b)$$

In the above equations the cyc. perm. represent cyclic permutations of the wave vectors  $\mathbf{k}_1$ ,  $\mathbf{k}_2$  and  $\mathbf{k}_3$ .

To evaluate  $B_{\nu\nu c}$  we expand the terms perturbatively. Employing tree level perturbation theory, the contributions from  $B_{\nu\nu c,112}$  are from these terms:

$$B_{\nu\nu c} = B_{\nu\nu c,112}(\mathbf{k}_1, \mathbf{k}_2, \mathbf{k}_3) + B_{\nu\nu c,112}(\mathbf{k}_2, \mathbf{k}_3, \mathbf{k}_1) + B_{\nu\nu c,112}(\mathbf{k}_1, \mathbf{k}_2, \mathbf{k}_3). \quad (58)$$

In our notation,  $B_{\nu\nu c,112}(\mathbf{k}_1, \mathbf{k}_2, \mathbf{k}_3) \equiv \langle \delta_\nu^{(1)}(\mathbf{k}_1) \delta_\nu^{(1)}(\mathbf{k}_2) \delta_c^{(2)}(\mathbf{k}_3) \rangle$  and similarly for the other terms. In terms of the second-order kernels  $F_2(\mathbf{k}_1, \mathbf{k}_2)$  we have:

$$B_{\nu\nu c,112}(\mathbf{k}_1, \mathbf{k}_2, \mathbf{k}_3) = 2F_2(\mathbf{k}_1, \mathbf{k}_2)P_{\nu c}(k_1)P_{\nu c}(k_2); \quad (59)$$

The other terms can be recovered by cyclic permutation of the wavenumber. In the squeezed limit we have:

$$B_{\nu\nu c}^{2D,\text{sq}} = \left[ \frac{24}{7} - \frac{1}{2} \frac{d \ln k^2 P_{\nu c}(k_\perp)}{d \ln k_\perp} \right] P_{\nu c}(k_\perp) P_{\nu c}(q_{3\perp}). \quad (60)$$

Finally we turn to  $B_{cc\nu}$ . The perturbative contributions are as follows:

$$B_{\nu\nu c}^{2D,\text{sq}} = 2[F_2(\mathbf{k}_1, \mathbf{k}_2)P_{cc}(k_1)P_{c\nu}(k_2) + \text{cyc.perm.}]. \quad (61)$$

Going through an elaborate algebraic manipulation we arrive at the squeezed limit:

$$B_{\nu\nu c}^{2D,\text{sq}} = \left[ \frac{24}{7} - \frac{1}{2} \frac{d \ln k^2 P_{cc}(k_\perp)}{d \ln k_\perp} \right] P_{cc}(k_\perp) P_{cc}(q_{3\perp}) + \left[ \frac{24}{7} - \frac{1}{2} \frac{d k_\perp^2 P_{c\nu}(k_\perp)}{d \ln k_\perp} \right] P_{c\nu}(k_\perp) P_{cc}(q_{3\perp}). \quad (62)$$

In future it will be interesting to study the effect of neutrino mass on bispectrum using simulations when all-sky lensing maps for such cosmologies will be available (Liu et al. 2018; Coulton et al. 2018).

## 10.5 Clustering Quintessence

Quintessence (Tsujikawa 2013) is the most popular dynamics of dark energy in which the potential energy of a single scalar field drives the accelerated expansion of the Universe. The quintessence model is different from the cosmological constant scenario allowing for a different temporal dependence of the observables. The scalar field in most quintessence models is considered homogeneous and is typically minimally coupled. The sound speed of the scalar field in these models equals the speed of light which prevents any clustering below the horizon scale. However, extensions of such models with vanishing or lower than speed of light have also been considered. These models are known as the clustering quintessence models (Sefusatti & Vernizzi 2011; Bassel et al. 2001). The future large scale structure surveys can be used to differentiate between these two scenarios. We use our formalism to derive the changes in the bispectrum in the squeezed limit in these models. We quote the expression of the kernel  $F_2$  from (Sefusatti & Vernizzi 2011):

$$\frac{D_+}{a} = \frac{5}{2} \Omega_M \left[ \Omega_M^{4/7} + \frac{3}{2} \Omega_M + \left( \frac{1}{70} - \frac{1+w}{4} \right) \Omega_Q \left( 1 + \frac{\Omega_M}{2} \right) \right]^{-1}. \quad (63a)$$

Here,  $\Omega_Q$  and  $\Omega_M$  are the density parameter related to Quintessence and dark matter. The corresponding linear growth rates are denoted by  $D_{Q+}$  and  $D_+$ . The parameters  $\epsilon_s = \frac{\Omega_Q}{\Omega_M} \frac{D_{Q+}}{D_+}$  and  $\nu_2$  can also be expressed in terms of  $\Omega_Q$  and  $\Omega_M$  and depend of redshift  $z$ .

$$F_2(\mathbf{k}_1, \mathbf{k}_2, \eta) = \frac{\nu_s}{2} + \frac{1}{2}(1 - \epsilon_s) \frac{\mathbf{k}_1 \cdot \mathbf{k}_2}{k_1 k_2} \left( \frac{k_1}{k_2} + \frac{k_2}{k_1} \right) - \frac{1}{2} \left( 1 - \epsilon_s - \frac{\nu_s}{2} \right) \left[ 1 - 3 \left( \frac{\mathbf{k}_1 \cdot \mathbf{k}_2}{k_1 k_2} \right)^2 \right]. \quad (64a)$$

Thus, two different parameters  $\epsilon_s(z)$  and  $\nu_s(z)$  to describe the tree-level bispectrum in this model.

$$C_{21} = \int_0^{r_s} dr \frac{w^3(r)}{d^{4+2n}(r)} D_+^4(z) \left[ \frac{1}{4}(1 - \epsilon_s) + \frac{3}{8}\nu_s - \frac{1}{2}(1 - \epsilon_s)(n+2) \right] \left/ \left( \int_0^{r_s} dr \frac{w^2(r)}{d^{2+n}(r)} D_+^2(z) \right)^2 \right. \quad (65a)$$

Typically at low redshift for some values of  $w$  the parameter  $\epsilon$  can reach upto 10% which can lead to roughly an order of 10% correction to the bispectrum which can be accounted for high precision measurements from future surveys.

## 10.6 Bispectrum in General Scalar-tensor Theories

Next, we consider a phenomenological fitting function. The second-order perturbative analysis of the general scalar tensor theories were initially performed by (Hirano, Kobayashi, Tashiro, Yokoyama 2017) which was later extended to smaller non-perturbative scales using a fitting function (Namikawa, Bouchet & Taruya 2018). Using the fitting function proposed in (Namikawa, Bouchet & Taruya 2018) we can compute the  $C_{21}$  in a class of models which are represented by the following expression for  $F_2(\mathbf{k}_1, \mathbf{k}_2, z)$  replacing  $F_2(\mathbf{k}_1, \mathbf{k}_2)$  in Eq.(1c):

$$F_2(\mathbf{k}_1, \mathbf{k}_2, z) = \left[ \kappa_s(z) - \frac{2}{7} \lambda_s(z) \right] a(k_1, z) a(k_2, z) + \frac{1}{2} \kappa_s(z) \left[ \frac{\mathbf{k}_1 \cdot \mathbf{k}_2}{k_1 k_2} \right] \left( \frac{k_1}{k_2} + \frac{k_2}{k_1} \right) b(k_1, z) b(k_2, z) \\ + \frac{2}{7} \lambda(z) \left[ \frac{\mathbf{k}_1 \cdot \mathbf{k}_2}{k_1 k_2} \right]^2 c(k_1, z) c(k_2, z); \quad (66a)$$

$$\lambda_s(z) = [\Omega_M(z)]^{\xi_\lambda}; \quad \kappa_s(z) = [\Omega_M(z)]^{\xi_\kappa}; \quad \Omega_M(z) = \Omega_{M,0}(1+z)^3 / ((1+z)^3 \Omega_{M,0} + \Omega_\Lambda). \quad (66b)$$

The functions  $\kappa_s(z)$  and  $\lambda(z)$  are approximated using the above functional forms and  $\xi_\lambda$  and are free parameters that can be estimated from observational data. The functional forms for  $a, b$  and  $c$  are assumed to be same as that of their  $\Lambda$ CDM form (Scoccimarro & Couchman 2001; Gil-Marín et al. 2011) which interpolates the perturbative regime and highly nonlinear assumed to be described by Hyper-Extended-Perturbation-Theory (Scoccimarro & Frieman 2012). To be consistent with the literature we have used  $\kappa_s$  to denote one of the parameters which should not be confused with the weak lensing convergence  $\kappa$  as their meaning would be obvious from the context. For  $\kappa_s(a) = 1$  and  $\lambda_s(a) = 1$  or, equivalently,  $\xi_\kappa = 0$  and  $\xi_\lambda = 0$  we recover the case of General Relativity (GR) presented in Eq.(1c). As discussed before, the Horndeski theories are the most general class of scalar-tensor theories which are non-degenerate that leads second-order equations of motion in 4D. In these models,  $\lambda_s \neq 1$  though  $\kappa = 1$  still remains valid. A generalization of Horndeski (Horndeski 1974) theory leads to a class of models that are known as “Beyond Horndeski” models (Gleyzes et al. 2015a,b; Langaïs & Noui 2016). In his models both  $\kappa_s$  and  $\lambda_s$  can deviate from unity. At high- $z$  the both theories converge to GR as expected. The Horndeski theories violate the Vainshtein mechanism to recover GR at nonlinear scale has also been considered. In these scenarios the parameter both  $\kappa$  and  $\lambda$  deviates from unity. Thus testing GR which correspond to  $\lambda = \kappa = 1$  reduces to constrain deviation of  $\lambda$  and  $\kappa$  from unity. The functional form for  $\kappa$  and  $\lambda$  is adopted from (Namikawa et al. 2018) and converges to GR at high- $z$  as expected.

We will next focus on computing the second order vertex  $\nu_2$  as defined in Eq.(21) for both 3D and 2D. Unlike in case of GR, in general these vertices have a redshift dependence. To compute these we start by noticing that in both three and two dimensions we have  $\langle \mathbf{k}_1 \cdot \mathbf{k}_2 / k_1 k_2 \rangle = 0$  and in 2D we have  $\langle (\mathbf{k}_1 \cdot \mathbf{k}_2 / k_1 k_2)^2 \rangle = 1/2$ . In the following, we will ignore smoothing as the correction terms involved will be exactly same as the one presented

In the quasilinear regime the functions  $a, b$  and  $c$  tend to unity. In this limiting case the departure from GR is encoded only in the redshift dependent factors and the expression for  $C_{21}$  is identical to Eq.(49) with the specific form for  $\kappa_s$  and  $\lambda_s$  are given by Eq.(66b). Substituting  $\kappa_s(z) = 1$  and  $\lambda_s(z) = 1$  we recover the unsmoothed results for GR. The smoothing in 3D and 2D will introduce terms involving factors of  $(n+3)$  in Eq.(40a)-Eq.(40b) and  $(n+2)$  in Eq.(26a)-Eq.(27b). The results for specific models for 3D and 2D are respectively shown in Figure-4 and Figure-5. While for GR the  $\langle F_2 \rangle$  is independent of redshift  $z$ , for Horndeski and beyond Horndeski theories  $\langle F_2 \rangle$  depends on redshift. At higher  $z$  they become identical to that of GR as expected. In Figure-4 the  $\langle F_2 \rangle$  for the 2D cylindrical collapse is plotted as function of  $z$  and their pattern of evolution is same as in 3D. The effect of line-of-sight projection is encoded in the factor  $R_2(z)$  which is shown in the right panel.

Although, the results for higher-order spectra are known to an arbitrary order in GR, similar results for most of the modified gravity theories are known mostly to second order. Going beyond third-order in general requires order-by-order calculation. While we have considered the statistics of 3D density field  $\delta$  and resulting convergence  $\kappa$  similar results can be obtained for the divergence of peculiar velocity.

The tests involving bispectrum related statistics presented here can further tighten the constraints obtained using linear growth rate alone. This is particularly important as no strong constraint on  $\lambda_s$  and  $\kappa_s$  exist currently. Indeed, there are no upper or lower limits for  $\kappa_s$  based on theoretical expectation.

Before we conclude this section, we would like to point out that the two parameters used in defining the clustering quintessence i.e.  $\nu_s$  and  $\epsilon_s$  (or  $\alpha_s$  and  $\beta_s$  for the case of DHOST theories) can independently be constrained using 3D and 2D measurements. This is due

to the fact that the statistics  $C_{21}$  depends on  $\nu_s$  and  $\epsilon$  in a different manner in 3D and 2D. We have concentrated on projected or 2D surveys in this paper but similar results will be presented for 3D surveys in a separate article.

## 11 CONCLUSIONS AND FUTURE PROSPECTS

We have computed the skew-spectrum (see Eq.(10a)) and kurtosis-spectrum Eq.(15a)) at low  $\ell$  for the analysis of weak lensing convergence or  $\kappa$  maps. These spectra generalize the one-point cumulants, e.g. the skewness and kurtosis defined in §3, and are often used in the literature for analyzing higher-order non-Gaussianity of cosmological maps. They capture some of the essential properties of the full bispectrum or trispectrum which are more difficult to estimate. In the real space these spectra correspond to cumulant correlators that can be computed in the leading-order using tree-level perturbations in the large-separation limit. In this limit these spectra can be computed to arbitrary order using tree-level perturbative calculations without any need for any phenomenological fitting functions or extensions of perturbative calculation. We use the flat-sky approximation and Eulerian perturbative results based on generating function approach we show how to compute high-order spectra to arbitrary order. We test these results for lower-order spectra namely the skew- and kurt-spectra against state-of-the-art all-sky weak lensing maps. We find our results are in good agreement. These results will be valuable in analyzing higher-order statistics from future all-sky weak lensing surveys such as the *Euclid* survey. The presence of mask generated from near all-sky surveys introduces mode mixing. Unless corrected, the mode mixing introduced by a mask can be a source of confusion while analyzing the higher-order spectra as they encode information about gravity induced mode-coupling. We have presented a generalization of existing method typically used in the study of ordinary power spectrum to construct unbiased estimates of higher-order spectra Eq.(41a)-Eq.(41b).

The parameters  $C_{pq}$  computed for 3D weak lensing will be important when photo- $z$  information is available. The statistics introduced here will be useful in analyzing non-Gaussianity in such context. We will present results of such analysis in future work. The results presented here can be generalized using a 3D Fourier-Bessel transform or a 3D flat sky formalism. As noted before the 3D analysis allows factorization  $C_{pq} = C_{pq} C_{q1}$  and their dependence on the spectral index  $n$  are different so 2D and 3D results will provide independent information as well as much needed consistency checks and test for possible systematics.

Any modification of gravity leaves detectable signature at the level of bispectrum. Though such signatures are less prominent than any modification at the level of power spectrum, it has recently attracted a lot of attention in the context of CMB lensing bispectrum (Namikawa et al. 2018). Similar investigations in the context of weak lensing are currently being pursued using various statistical estimators. Various techniques were adopted to extend perturbative results derived in the context of General Relativity (GR). Extensions to modified gravity scenarios were implemented by introducing more freedom to the kernels and calibrating then using numerical simulations (Bose & Taruya 2018). The expressions for bispectrum exist for both type of modified gravity scenarios i.e. models with Vainshtein-screening mechanism which includes the DGP model as well as the Horndeski (Hordenski 1974) and beyond Horndeski theories (Gleyzes et al. 2015a,b; Langois & Noui 2016). In the other class of models i.e. models with Chameleon-screening that includes the Hu-Sawicki  $f(R)$  model (Hu & Sawicki 2016) the bispectrum from simulations can be successfully reproduced using the GR expression but with suitable modification of the power spectrum. We will extend our results derived here to the modifying gravity scenarios as well as scenarios involving massive neutrinos.

The position-dependent bispectrum and its higher-order generalization at the level of trispectrum has exact one-to-one correspondence with the statistics studied in this paper. Indeed the expressions for integrated bispectrum and the skew-spectrum at low- $\ell$  are identical. However, the physical interpretation is different. The expressions at the level of fourth order are not the same. The integrated bispectrum or equivalently the position-dependent power spectrum probes the influence of large scale modes on small-scale structure. The cumulant correlators at large separation limit as well as their harmonic counterparts namely the skew-spectrum and kurt-spectra probe dynamics mainly at scales of smoothing. Comparing results from these two statistics can provide useful cross-checks at each order.

Finite sky coverage can introduce bias in our estimators. The scatter and bias introduced by finite survey size have been studied in great detail for galaxy surveys and to a lesser extent for weak lensing surveys (Munshi & Coles 2003). These are less dominant in the quasi-linear regime where the variance is small in the limiting case which we have studied here.

In our study we have assumed that the bispectrum is of even parity. Many studies in the recent past have pointed out existence of an off-parity bispectrum (Munshi et al. 2012). Such a bispectrum do not arise from 3D density perturbations. However, signatures of contributions can be used to test possible existence of systematics.

In a recent work (Barthelemy 2019), it was shown that *nulling* can be used effectively to improve the accuracy of perturbative calculations by reducing the cross-talk between quasilinear and nonlinear scales. These calculations were performed in the real-space

focusing primarily on one-point cumulants and PDF. In contrast our results here concern primarily on two-point correlators and their associated spectra in the Fourier domain. Applying the nulling before computing the spectra is expected to improve the validity of the perturbative results.

Last but not least, the next generation of CMB Stage-IV experiments will be able to map the projected lensing potential all the way to the surface of last scattering. It is expected that the results obtained in this paper will be valuable in analyzing higher-order statistics of maps obtained from such experiments (Abajazian et al. 2018). However, in this case the estimator described here will have to be optimized to tackle low signal-to-noise for higher-order statistics of CMBR. The post-born corrections (Lewis & Pratten 2016) play an important role in higher-order statistics of CMBR. For realistic comparison against observations such corrections should be included.

## ACKNOWLEDGMENT

DM is supported by a grant from the Leverhume Trust at MSSL. It is a pleasure for DM to thank F. Bouchet, T. D. Kitching, T. Namikawa, R. Takahashi, A. Taruya and F. Vernizzi for many useful discussions. We would like to also thank R. Takahashi for making the lensing maps publicly available. We would like to also thank R. Schoenrich for careful reading of the draft and many suggestions that greatly improved the presentation. DM would also like to organizers of the Euclid Theory Working Group Meeting (8th April - 9th, April 2019) in Oxford.

## REFERENCES

- K. Abajazian et al. [arXiv/1907.04437]  
 T. Abbott, F. B. Abdalla, S. Allam, et al., 2016, *Pjys. Rev. D*, 94, 022001 [arxiv/1507.0552]  
 Virgo, LIGO Scientific Collaboration, B. P. Abbott et. al., 2017, *PRL*, 119, 161101, 1710.05832. [arXiv/1710.05832]  
 M. Asgari, A. Taylor, B. Joachimi, T. D. Kitching [arXiv/1612.04664]  
 L. Amendola et al., 2013, *Living Rev. Relativity* 16, 6, [arXiv/1206.1225].  
 R. Balian, R. Schaeffer, 1989, *A&A*, 220, 1  
 A. Barthelemy, S. Codis, C. Uhlemann, F. Bernardeau, R. Gavazzi [arXiv/1909.02615]  
 N. Bartolo, E. Komatsu, S. Matarrese, A. Riotto, 2004, *Physics Report*, 402, 103 [astro-ph/0406398]  
 T. Baker et al. 2017, *Phys. Rev. Lett.* 119, 251301 [arXiv/1510.06930]  
 T. Basse, O. E. Bjelde, Y. Y. Y. Wong [arxiv/1009.0010]  
 F. Bernardeau, 1992, *ApJ*, 392, 1  
 F. Bernardeau, 1994, *A&A*, 291, 697, [astro-ph/9403020]  
 F. Bernardeau, 1994, *ApJ*, 427, 51 [astro-ph/9311066]  
 F. Bernardeau 1995, *A&A*, 301, 309 [arXiv/9502089]  
 F. Bernardeau, 1994, *ApJ*, 433, 1 [astro-ph/9312026]  
 F. Bernardeau 1996, *A&A*, 312, 11 [arXiv/9602072]  
 F. Bernardeau, 1996, *A&A*, 312, 11 [astro-ph/9602072]  
 F. Bernardeau, P. Brax 2011, *JCAP*, 1106, 019 [arXiv/1102.1907]  
 F. Bernardeau, P. Reimberg, 2016, *Phys. Rev. D* 94, 063520 [arXiv/1511.08641]  
 F. Bernardeau, Y. Mellier, L. van Waerbeke, 2002, *A&A*, 389, L28 [astro-ph/0201032].  
 F. Bernardeau, S. Colombi, E. Gaztanaga, R. Scoccimarro, 2002, *Physics Report*, 367, 1, [astro-ph/0112551]  
 F. Bernardeau, L. van Waerbeke, Y. Mellier, 2003, *A&A*, 397, 405 [astro-ph/0201029]  
 B. Bose, A. Taruya, 2018, *JCAP*, 1810, 2018, 019 [astro-ph/1808.01120]  
 E. Calabrese, J. Smidt, A. Amblard, A. Cooray, A. Melchiorri, P. Serra, A. Heavens, D. Munshi, 2010, *Phys. Rev. D*, 81, 3529 [0909.1837]  
 P. G. Castro, A. F. Heavens, T. D. Kitching, 2005, *Phys. Rev. D* 72, 023516 [astro-ph/0503479]  
 W. R. Coulton, J. Liu, M. S. Madhavacheril, V. Bhm, D. N. Spergel, [arXiv/1810.02374]  
 T. Clifton, P. G. Ferreira, A. Padilla, C. Skordis, 2012, *Physics Report* 513, 1, 1, [astro-ph/1106.2476]  
 P. Creminelli, F. Vernizzi, 2017, *Phys. Rev. Lett.* 119, 251302, [arXiv/1710.05877]  
 M. Crisostomi, M. Lewandowski, F. Vernizzi, 2019, *Phys. Rev. D* 100, 024025, [arXiv/1903.11591]

- M. Crisostomi, M. Lewandowski, F. Vernizzi1 [arXiv/1909.07366]
- A. Cooray, R. Sheth, 2002, *Physics Report*, 372, 1, [arXiv/0206508].
- G. Cusina, M. Lewandowski, F. Vernizzi, 2018, *JCAP*, 04, 005, [arXiv/1712.02783]
- G. Cusina, M. Lewandowski, F. Vernizzi, 2018, *JCAP*, 04, 005, [arXiv/1710.05877]
- G. Dvali, G. Gabadadze, M. Porrati, 2000, *Phys. Rev. B*, 485, 208, [arXiv/1510.06930]
- C. Deffayet, X. Gao, D. A. Steer, G. Zahariade, 2011, *Phys. Rev. D*, 84, 064039, [arXiv/1103.3260]
- G. Efstathiou, 2004, *MNRAS*, 349, 603, [astro-ph/0307515]
- A. Eggemeier, R. E. Smith, 2017, *MNRAS*, 466, 2496, [arXiv/1611.01160].
- D. J. Eisenstein, D. H. Weinberg, E. Agol, et al. 2011, *AJ*, 142, 72, [astro-ph/1101.1529]
- E. Gaztanaga, F. Bernardeau 1998, *A&A*, 331, 829 [arXiv/9707095]
- H. Gil-Marn, C. Wagner, F. Frangkoudi, R. Jimenez, L. Verde, [arXiv/1111.4477]
- A. Goldstein et. al., *ApJ*, 2017, 848, L14, [arXiv/1710.05446]
- K. M. Gorski, E. Hivon, A. J. Banday, B. D. Wandelt, F. K. Hansen, M. Reinecke, M. Bartelman, 2005, *ApJ*, .622, 759, [astro-ph/0409513]
- I. Harrison, P. Coles, 2011, *MNRAS* 418, L20, [arXiv/1108.1358]
- A. F. Heavens, S. Gupta, 2001, *MNRAS*, 324, 960, [astro-ph/1610.02956]
- G. W. Horndeski, 1974, *International Journal of Theoretical Physics*, 10, 363,
- J. Gleyzes, D. Langlois, F. Piazza, F. Vernizzi, 2015, *JCAP*, 2, 018, [arXiv/1408.1952]
- J. Gleyzes, D. Langlois, F. Piazza, F. Vernizzi, 2015, *Phys. Rev. Lett.*, 114, 211101, [arXiv/1404.6495]
- S. Hirano, T. Kobayashi, H. Tashiro, S. Yokoyama, 2018, *Phys. Rev. D* 97, 103517, [arXiv/1801.07885].
- E. Hivon, K. M. Gorski, C. B. Netterfield, B. P. Crill, S. Prunet, F. Hansen, 2002, *ApJ*, 567, 2, [astro-ph/0105302]
- C. Hikage, M. Takada, T. Hamana, D. Spergel, 2011, *MNRAS*, 412, 65, [arXiv/1004.3542]
- G. W. Horndeski, 1974, *International Journal of Theoretical Physics*, 10, 363.
- W. Hu, 2001, *Phys. Rev. D*, 64, 083005, [arXiv/0151117]
- W. Hu, I. Sawicki, 2007, *Phys. Rev. D*, 76, 064004, [arXiv/0705.1158]
- R. J. Jurek, C. Blake, et al. 2010, *MNRAS*, 401, 14, [astro-ph/0911.4246]
- A. Joyce, B. Jain, J. Khoury, M. Trodden, 2015, *Physics Report*, 568, 1, [astro-ph/1407.0059]
- T. D. Kitching, A. F. Heavens, 2017, *Phys. Rev. D* 95, 063522 [arXiv/1612.00770]
- K. Koyama, A. Taruya, T. Hiramatsu, 2009, *Phys. Rev.*, D79, 123512, [arXiv/0902.0618]
- T. Kobayashi, M. Yamaguchi, J. Yokoyama, 2011, *Progress of Theoretical Physics* 126, 511, [arXiv/1105.5723]
- K. Kuijken, C. Heymans, H. Hildebrandt, et al. 2015, *MNRAS*, 454, 3500, [astro-ph/1507.00738]
- D. Langlois, K. Noui, 2016, *JCAP*, 2, 034, [arXiv/1510.06930]
- D. Langlois, K. Noui, 2016, *JCAP*, 7, 16, [arXiv/1512.06820]
- D. Langlois, K. Noui, 2016, *Cosmol. Astropart. Phys.* 02, 034, [arXiv/1510.06930]
- R. Laureijs, J. Amiaux, S. Arduini, et al., 2011, *ESA/SRE(2011)12*
- J. Lesgourgues, S. Pastor, 2006, *Physics Report*, 429, 307,
- E. L. Lokas, R. Juszkiewicz, D. H. Weinberg, F. R. Bouchet, 1995, *MNRAS*, 274, 3 [astro-ph/9508032]
- L. Lombriser, N. A. Lima 2017, *Phys. Lett. B* 765, 382 [arXiv/1602.07670]
- J. Liu, S. Bird, J. M. Z. Matilla, J. C. Hill, Z. Haiman, M. S. Madhavacheril, D. N. Spergel, A. Petri, 2018, *JCAP* [arXiv/1711.10524]
- T. Matsubara, 2007, *ApJS*, 170, 1, [astro-ph/0610536]
- T. Matsubara, 2003, *ApJ*, 584, 1, [astro-ph/0006269]
- D. Munshi, V. Sahni, A. A. Starobinsky, 1994, *ApJ*, 436, 517, [arXiv/9402065]
- D. Munshi, F. Bernardeau, A. L. Melott, R. Schaeffer, 1999, *MNRAS*, 303, 433, [arXiv/9707009]
- D. Munshi, P. Coles, A. L. Melott, 1999, *MNRAS*, 310, 892, [arXiv/9902215]
- D. Munshi, 2000, *MNRAS*, 318, 145, [astro-ph/0001240]
- D. Munshi, B. Jain, 2000, *MNRAS*, 318, 109, [astro-ph/9911502]
- D. Munshi, B. Jain, 2001, *MNRAS*, 322, 107, [astro-ph/9912330]
- D. Munshi, P. Coles, 2003, *MNRAS*, 338, 846, 856, [astro-ph/0003481]
- D. Munshi, P. Valageas, L. Van Waerbeke, A. Heavens, 2008, *Physics Report*, 462, 67, [arXiv:0612667]
- D. Munshi, P. Coles, A. Cooray, A. Heavens, J. Smidt, 2011, *MNRAS*, 410, 1295, [1002.4998]

- D. Munshi, A. Heavens, 2010, MNRAS, 401, 2406, [astro-ph/0001240].
- D. Munshi, J. Smidt, A. Heavens, P. Coles, A. Cooray, 2011, MNRAS, 411, 2241, [0910.3693]
- D. Munshi, P. Valageas, A. Cooray, A. Heavens, 2011, MNRAS, 414, 3173, [arXiv/0910.3693].
- D. Munshi, J. Smidt, A. Heavens, P. Coles, A. Cooray, 2011, MNRAS, 411, 2241, [1003.5003].
- D. Munshi, A. Heavens, A. Cooray, J. Smidt, P. Coles, P. Serra, 2011, MNRAS, 412, 1993, [0910.3693].
- D. Munshi, P. Coles, A. Cooray, A. Heavens, J. Smidt, 2011, MNRAS, 414, 3173, [arXiv/1002.4998]
- D. Munshi, L. van Waerbeke, J. Smidt, P. Coles 2012, MNRAS, 419, 536 [1103.1876]
- D. Munshi, J. Smidt, A. Cooray, A. Renzi, A. Heavens, P. Coles 2013, MNRAS, 434, 2830 [1011.5224]
- D. Munshi, 2017, JCAP, 01, 049, [arXiv/1610.02956]
- D. Munshi, T. Kitching, A. Heavens, P. Coles, 2011, MNRAS, 416, 629, [arXiv/1711.04767]
- D. Munshi, T. Namikawa, T. D. Kitching, J. D. McEwen, R. Takahashi,  
F. R. Bouchet, A. Taruya, B. Bose, 2020, MNRAS, 493, 3985, [arXiv/1910.04627]
- D. Munshi, J. D. McEwen, T. Kitching, P. Fosalba, R. Teyssier, J. Stadel, [arXiv/1902.04877]
- National Research Council. 2010. New Worlds, New Horizons in A&A. The National Academies Press. DDDDDD [New Horizons]
- T. Namikawa, B. Bose, F. R. Bouchet, R. Takahashi, A. Taruya, 2019, Phys. Rev. D, 99, 063511, [arxiv/1812.10635]
- T. Namikawa, F. R. Bouchet, A. Taruya, [astro-ph/1805.10567]
- T. Okamoto, W. Hu 2002, Phys. Rev. D, 66, 063008 [arXiv/0206155]
- S. P. Oh, D. N. Spergel, G. Hinshaw 1990, ApJ, 510, 551 [astro-ph/9805339]
- A. Peel, C.-A. Lin, F. Lanusse, A. Leonard, J.-L. Starck, M. Kilbinger, 2017, A&A, 599, 79, [arXiv/1612.02264]
- M. Peloso, M. Pietroni 2014, JCAP, 04, 011 [astro-ph/0612667]
- Planck Collaboration, 2014, A&A, 571, A16, [astro-ph/1303.5076]
- Planck Collaboration, 2016, A&A 594, A13, [astro-ph/1502.01589]
- Planck collaboration, 2016, A&A, 594, A17, [astro-ph/1502.01592].
- Planck Collaboration, 2018, [arXiv/1807.06205]
- G. Pratten, A. Lewis 2016, JCAP, 08, 047 [arXiv/1905.1136]
- M. A. Riquelme, D. N. Spergel, 2007, ApJ, 661, 672, [1002.4998]
- R. Ruggeri, E. Castorina, C. Carbone, E. Sefusatti 2018, JCAP, 03, 003 [arXiv/1712.02334]
- J. Sakstein, B. Jain 2017, Phys. Rev. Lett. 119, 251303 [arXiv/1710.05893]
- R. Scoccimarro, H. M. P. Couchman, 2001, MNRAS, 325, 4 [arXiv/0902.0618]
- R. Scoccimarro, J. A. Frieman, 1999, ApJ, 520, 35, [astro-ph/9811184]
- E. Sefusatti, F. Vernizzi 2011, JCAP, 1103, 047 [arXiv/1101.1026]
- J. Smidt, A. Amblard, C. T. Byrnes, A. Cooray, A. Heavens, D. Munshi 2010, Phys. Rev. D, 81, 123007, [0909.1837].
- I. Szapudi S. Prunet, D. Pogosyan, A. S. Szalay, J. R. Bond, 2001, ApJ, 548, 115
- I. Szapudi, A. S. Szalay 1999, ApJ, 515, L43 [arXiv/9702015]
- R. Takahashi, T. Hamana, M. Shirasaki, T. Namikawa,  
T. Nishimichi, K. Osato, K. Shiroshima, 2017, ApJ, 850, 24 [astro-ph/1706.01472]
- S. Tsujikawa 2013, Class.Quant.Grav., 30, 214003 [astro-ph/1304.1961]
- J. A. Tyson, D. M. Wittman, J. F. Hennawi, D. N. Spergel, 2003, Nuclear Physics B Proceedings Supplements, 124, 21 [astro-ph/0209632]
- P. Reimberg, F. Bernardeau 2018, Phys. Rev. D 97, 023524 [arXiv/1708.00252]
- C. Uhlemann, S. Codis, C. Pichon, F. Bernardeau, P. Reimberg 2016, MNRAS, 460, 1529 [arXiv/1512.05793]
- C. Uhlemann, C. Pichon, S. Codis, B. LHuillier, J. Kim, F. Bernardeau, C. Park, S. Prunet 2018, MNRAS, 477, 2772 [arXiv/1711.04767]
- A. J. Weiss, A. Schneider, R. Sgier, T. Kacprzak, A. Amara, A. Refregier, [arXiv/1905.1136]
- D. Munshi, P. Valageas, L. Van Waerbeke, A. Heavens Phys.Rept, 462, 67, 2008 [astro-ph/0612667]